NOTES 15

GAS FILM LUBRICATION

Luis San Andrés
Mast-Childs Professor
Turbomachinery Laboratory
Texas A&M University

http://rotorlab.tamu.edu/me626

Dear reader, to refer this material use the following format

San Andrés, L., 2010, *Modern Lubrication Theory,* "Gas Film Lubrication," Notes 15, Texas A & M University Digital Libraries, http://repository.tamu.edu/handle/1969.1/93197 [access date]

Introduction

Microturbomachinery (MTM)[1] demands gas bearings to ensure compactness, lightweight and extreme temperature operation. Gas bearings with large stiffness and damping, and preferably of low cost will enable successful commercial applications. Gas film bearings offer advantages of low friction and reduced heat generation. These advantages enable their successful applications in air-cycle units for airplane cabins, high-precision instruments, auxiliary power units, and high-speed MTM. In addition, gas bearing systems do not require costly, complex sealing and lubricant circulation systems; hence ensuring system compactness, low weight and extreme temperature operation. Furthermore, these bearings eliminate process fluid contamination and are environmental friendly. Gas foil bearings are in use; however, their excessive cost, protected technology and lack of calibrated predictive tools have prevented widespread use in mass-produced applications.

Gas bearings have a low load carrying capacity and require a minute film thickness to accomplish their intended function. Thus, their fabrication and installation tends to be expensive and time consuming. Another disadvantage is poor damping because of the inherently low viscosity of the gas.

The literature on the analyses of gas bearing analyses is extensive, albeit experimental verification and successful commercial implementations have not always been reported. Gross [1] (1962) covers the fundamentals of analysis that span the fast development of gas bearing technology in the 1960's. Pan [2] gives a serious description of the analysis and performance of (rigid surface type) gas bearings summing knowledge until 1980. The textbook of Hamrock [3] (1994) provides comprehensive analyses for the static load performance of both thrust and radial gas bearings. Czolczynski [4] (1999) gives a comprehensive review of the analyses for prediction of frequency dependent force coefficients of gas bearings.

The last decade (2000s) has seen a rebirth of gas bearings, in particular gas foil bearings for MTM [5] and aerostatic gas bearings for spindle machines [6]. San Andrés et al. [7-16] report the results of a comprehensive research program, experimental and analytical, evaluating and developing cost effective reliable gas bearings for MTM.

[1] As per the IGTI (International Gas Turbine Institute), a microturbomachinery has power < 250 kW.

Types of gas bearings

Bearings in rotating machinery are of two types: (a) radial bearings supporting lateral loads including rotor weight, and (b) thrust bearings carrying axial loads. See Figure 1 for a few relevant gas bearing configurations. These loads can be either static or dynamic or both. Gas film bearings behave as mechanical elements that provide stiffness, damping and inertia force coefficients that, in conjunction with the structural parameters of a rotor, determine the stability and dynamic behavior of the entire rotor bearing system (RBS).

In a gas bearing, a film of gas, hereby liberally referred as the lubricant, separates the rotating component (a journal, for example) from the stationary part (a housing or stator). Hydrodynamic shear action from the moving component enables the generation of the lubricant wedge where a hydrodynamic pressure evolves to produce the reaction force opposing the externally applied load. Gas bearings operating under the hydrodynamic (self-acting) principle are, in general, of simple construction although at times difficult to manufacture and install because of the required minute film clearances. Other bearings employ external pressurization supplied through restrictors (orifices, slots or capillaries) to enable a hydrostatic action that separates the surfaces thus inducing journal or rotor lift without rotation, for example. Hydrostatic bearings are mechanically more complex than hydrodynamic bearings because of their additional supply ports; albeit their major advantage lies on their usage in applications without rotor spinning. This advantage must be weighed against the extra cost plus the need of an external source of pressurized gas. More importantly, in a hybrid bearing configuration, i.e., one where both hydrostatic and hydrodynamic operating principles act jointly, the external supply pressure is typically used to promote early rotor lift off thus reducing temporary rubs, avoiding wear of surfaces and extending bearing life.

There are (probably) as many types of gas bearing configurations as there are applications; that is, a gas bearing is selected to fulfill certain functions while keeping a cost low, including component fabrication and installation, and of course, operation. The archival literature features successful applications of gas bearings; often failing to notice that, in contrast to liquid lubricated bearings, gas bearings have inherent limitations that prevent their widespread usage as load support elements in (heavy) commercial machinery.

Gases, although chemically more stable than liquids, have an inherent low viscosity – one or two orders of magnitude lower than that of mineral oils for example. Recall that the load

carrying capacity (W) of a self-acting hydrodynamic film bearing is roughly proportional to $\left(\mu AU \Big/ h_{\min}^2 \right)$ [3] where μ is the lubricant viscosity, U is the surface speed, A is the area of action, and h_{min} is the minimum film thickness. Hence, in order to achieve a desired load capacity, a gas lubricated bearing replacing a similar size oil-lubricated bearing must operate at an exceedingly high surface speed (U) or with a minute film thickness (h). That is, hydrodynamic gas bearings are not intended for supporting rotating machinery that operates with relatively low surface speeds or if the film clearance or gap is too large. Hence, the need for accurate manufacturing of parts which increases both cost and makes installation complicated. Of course, externally pressurized (aerostatic) gas bearings can be used efficiently to carry loads at low or even zero surface speeds. However, aerostatic bearings require a source of pressurized gas which adds cost and complexity [1,6,10].

To enhance the hydrodynamic action, designers have produced a number of bearing configurations that exploit geometrical features such as steps, grooves, pockets and dimples, for example. Figure 1 shows several typical commercial gas bearing configurations. The bearing types with textured surfaces, known as (spiral) grooved bearings and herringbone journal bearings have been instrumental to the operation of gyroscopes for aircraft and satellite navigation [2], enabled non contacting gas face seal technology [7]; and more recently, allowed the revolution in digital storage hard-drive technology [17]. In these applications, static and dynamics loads are relatively low. Note that, for optimum load performance giving the maximum static (centering) stiffness, the depth of the machined steps or grooves or pockets is just equal or a little larger than the operating film gap or clearance, as will be demonstrated later. Until recently, these geometrical features were difficult to machine at low cost, except in certain materials like silicon-carbide for non-contacting face seals. However, current casting and manufacturing processes allow the manufacturing of these bearings (or seals) at a relatively low cost and with near identical performance in one or millions of pieces.

Other radial bearing configurations of interest, i.e., undergoing close scrutiny and commercial development, include bump-type foil bearings [5, 15, 18], flexure pivot tilting pad bearings [13], and (low cost) metal mesh foil bearings [19].

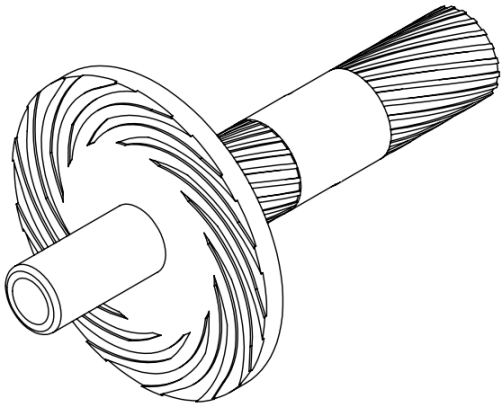

Spiral grooved thrust and radial bearings

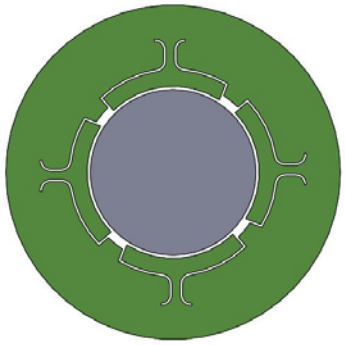

Flexure pivot tilting pad bearing

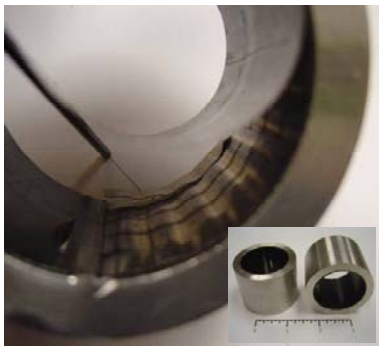

Bump-type foil bearing

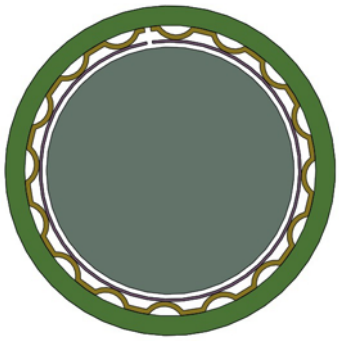

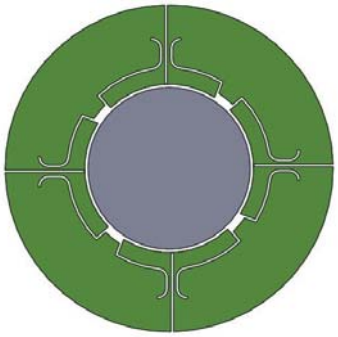

Flexure pivot tilting pad bearing with hydrostatic pressurization

Metal mesh foil bearing

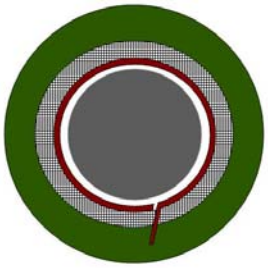

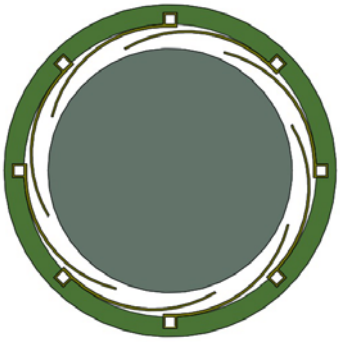

Overleaf-type foil bearing

Fig. 1 Typical commercial gas bearings for microturbomachinery

The fundamentals of gas film lubrication analysis

The fluid flow in a hydrodynamic gas bearing or gas face seal is typically laminar and inertialess, i.e. the Reynolds numbers $\mathrm{Re}=\rho U h/\mu <1$, because of the smallness in film thickness (h) and the low lubricant density (ρ). Gas annular seals, such as labyrinth and honeycomb types, are notable exceptions, since in these applications large pressure drops, high surface speeds and large clearances promote flow turbulence accompanied by strong fluid compressibility effects [20].

Consider, as shown in Figure 2, the flow of an ideal gas in a region confined between two surfaces separated by the small gap h. The top surface has velocity U along the x direction. For an isothermal process, the gas density (ρ) and pressure (p) are related by $\rho = \dfrac{p}{\Re_g \cdot T}$, with $\Re_g$ and T representing the gas constant and operating temperature, respectively.

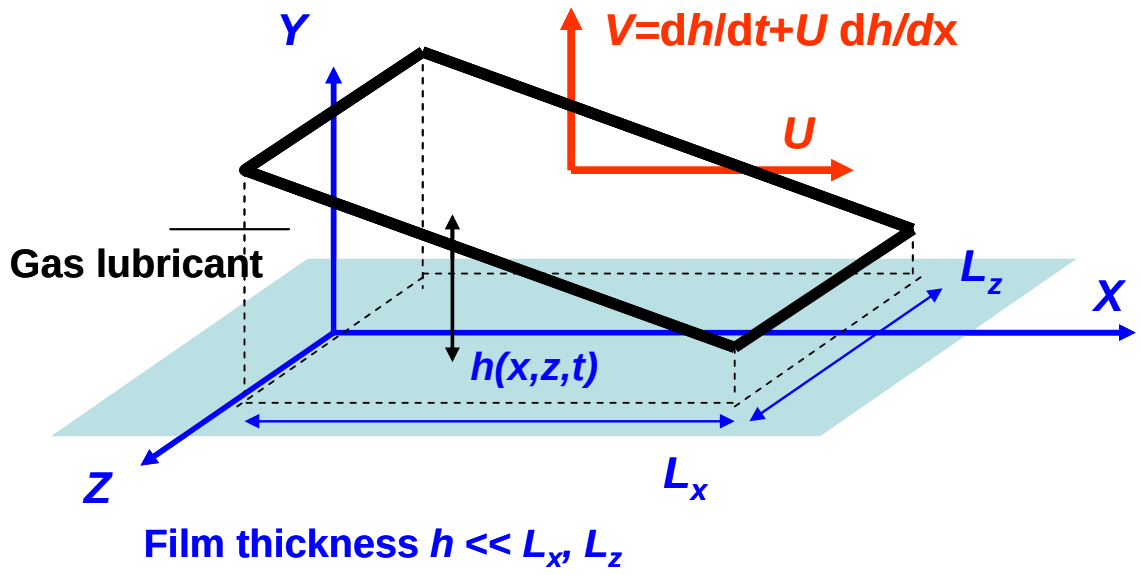

Fig. 2 Geometry of a gas lubricated thin film bearing

Table 1 shows a list of the physical properties of the most common gases used as lubricants in thin film bearings. The gas viscosity (μ) increases with its absolute temperature (T) as $\mu = \mu_o \dfrac{\left(1+\dfrac{T_*}{T_0}\right)}{\left(1+\dfrac{T_*}{T}\right)}\sqrt{\dfrac{T}{T_o}}$ where T_* and T_o are reference temperatures and $\mu_o = \mu(T_o)$.

Table 1. Viscosity and molecular weight of gases used in thin film bearings

Gas	formula	Molecular weight	μ_o μPa-s	T_o K	T^* K
Acetylene	C_2H_2	26.036	10.2	293	198
Air	O_2+N	29.000	17.1	273	124
Ammonia	NH_3	17.034	9.82	293	626
Argon	Ar	39.950	22.04	289	142
Carbon dioxide	CO_2	44.010	13.66	273	274
Carbon Monoxide	CO	28.010	16.65	273	101
Chlorine	Cl_2	70.900	12.94	289	351
Chloride	HCl	36.458	13.32	273	360
Helium	He	4.003	18.6	273	38
Hydrogen	H_2	2.016	8.5	273	83
Hydrogen sulfide	H_2S	34.086	12.51	290	331
Methane	CH_4	16.042	10.94	290	198
Neon	Ne	20.180	29.73	273	56
Nitrogen	N_2	28.020	16.65	273	103
Nitric Oxide	NO	30.010	17.97	273	162
Nitrous Oxide	N_2O	44.020	13.66	273	274
Oxygen	O_2	32.000	19.2	273	138
Steam	H_20	18.016	12.55	372	673
Sulfur Dioxide	SO_2	64.070	11.68	273	416
Xenon	Xe	131.300	21.01	273	220

Gas constant $\mathcal{R}_g = (8{,}314{,}34 \text{ J/kg-K})/MW$

Source: http://periodic.lanl.gov/default.htm

Reynolds equation describes the generation of the film pressure within the flow region [2].

$$\vec{\nabla}\cdot\left(\frac{-h^3 p}{12\mu}\cdot\vec{\nabla}\,p\right)+\frac{U}{2}\frac{\partial}{\partial x}(p\,h)+\frac{\partial}{\partial t}(p\,h)=0 \qquad (1)$$

Eq. (1) represents an isoviscous condition without fluid inertia effects. Furthermore, the derivation of Eq. (1) assumes the gas satisfies the no-slip condition, i.e. it adheres to the surfaces[2]. As a boundary condition, the pressure is typically ambient *(p_a)* on the boundary of the domain.

The gas film Reynolds equation is nonlinear; and hence exact solutions exist for a handful of limiting conditions [2,3]. The left hand side of the equation is elliptic in character, while the terms on the right hand side are known as the shear induced flow and squeeze film flow terms.

It is convenient to normalize Eq. (1) in terms of dimensionless variables and parameters. To this end, let

$$\overline{x} = \frac{x}{L_*}; \overline{z} = \frac{z}{L_*}; \tau = \omega t;\ H = \frac{h}{h_*};\ P = \frac{p}{p_a} \tag{2}$$

where L_* is a characteristic length of the bearing surfaces and h_* is a characteristic film thickness; typically the minimum film thickness or the clearance (c) in a radial bearing. Above ω denotes an excitation whirl frequency representative of unsteady or time transient effects. With the definitions given, Reynolds equation is written in dimensionless form as

$$\frac{\partial}{\partial \overline{x}}\left(P H^3 \frac{\partial P}{\partial \overline{x}} \right) + \frac{\partial}{\partial \overline{z}}\left(P H^3 \frac{\partial P}{\partial \overline{z}} \right) = \Lambda \frac{\partial}{\partial \overline{x}}\left(P H \right) + \sigma \frac{\partial}{\partial \tau}\left(P H \right) \tag{3}$$

where
$$\Lambda = \frac{6 \mu U L_*}{p_a h_*^2} \text{ and } \sigma = \frac{12 \mu \omega L_*^2}{p_a h_*^2} \tag{4}$$

are known as the speed number and the frequency number, respectively [2]. Both parameters represent the influence of fluid compressibility on the performance of the gas bearing. For Λ and σ small, typically < 1, the gas bearing operates as an incompressible fluid film bearing, as seen next.

For steady state applications, i.e., the film thickness (h) and the pressure (p) do not vary with time, and hence squeeze film effects are nil ($\sigma = 0$) . Eq. (3) reduces to

[2] As the film thickness (h) decreases into the nano meter scale, its size approaches that of the gas molecular free path (λ= 60 nm for air under standard conditions); and hence, slipping effects become significant. Magnetic recording and digital hard drive applications fall within this category. The Knudsen number (Kn= λ/h) aids to distinguish the flow regime of operation; Kn> 15 denotes molecular flow, 0.01< Kn< 15 represents slip flow, and Kn<0.01 gives a continuum flow, as in the applications discussed herein [21].

$$\frac{\partial}{\partial \bar{x}}\left(PH^3 \frac{\partial P}{\partial \bar{x}} \right) + \frac{\partial}{\partial \bar{z}}\left(PH^3 \frac{\partial P}{\partial \bar{z}} \right) = \Lambda \frac{\partial}{\partial \bar{x}}(PH) \tag{5}$$

For low speed numbers, Λ <<1, an expansion of the dimensionless pressure as $P = 1 + \Lambda \bar{P}$, and substitution into Eq. (5) gives the simplified Reynolds equation [2]

$$\frac{\partial}{\partial \bar{x}}\left(H^3 \frac{\partial \bar{P}}{\partial \bar{x}} \right) + \frac{\partial}{\partial \bar{z}}\left(H^3 \frac{\partial \bar{P})}{\partial \bar{z}} \right) = \frac{\partial}{\partial \bar{x}}(H) \tag{6}$$

which is formally identical to the Reynolds equation for an incompressible lubricant. Hence, its solution can be easily sought – analytically for either the short length or long journal bearings, or using numerical schemes for finite length bearings of any geometry. Refer to Lecture Notes 4 and 7 for details on the analytical and numerical solution of Eq. (6).

Clearly, the assumed solution is strictly valid for $\Lambda \to 0$. Hence, the pressure field cannot be much higher than ambient pressure (p_a), and consequently, the bearing load capacity is also small albeit proportional to the speed number, i.e. it increases linearly with surface speed (U), for example. Note that the dimensionless pressure $\bar{P} = \dfrac{P-1}{\Lambda} = \dfrac{(p - p_a) h_*^2}{6 \mu U L_*}$ as is typical in mineral oil lubricated bearings. Analytical solutions to Eq. (5) are available for either the short length or infinitely long cylindrical journal bearings, for example. Closed form solutions are also available for simple one-dimensional slider or Rayleigh-step bearing geometries, see Refs. [2, 21] for example.

On the other hand, for large speed numbers, Λ >>1, Eq. (5) is written as

$$\frac{1}{\Lambda}\left[\frac{\partial}{\partial \bar{x}}\left(PH^3 \frac{\partial P}{\partial \bar{x}} \right) + \frac{\partial}{\partial \bar{z}}\left(PH^3 \frac{\partial P}{\partial \bar{z}} \right) \right] = \frac{\partial}{\partial \bar{x}}(PH) \tag{7}$$

and, in the limit $\Lambda \to \infty$, the left hand side of the equation can be neglected to obtain[3]

$$\frac{\partial}{\partial \bar{x}}(PH) = 0 \Rightarrow p = p_a \frac{h_b}{h(x)} \tag{8}$$

where h_b is the film thickness at the boundary where the pressure is ambient. The limiting speed solution, Eq. (8) above, shows that the pressure within the film is bounded and independent of the surface speed U. This result is in opposition to that in incompressible fluid bearings where

[3] The *PH* solution is an inner field which must be matched to an outer (boundary) solution satisfying the side pressure condition (P=1) [2]. For the purposes of this review, the *PH* solution is adequate.

the generated hydrodynamic film pressure is proportional to the surface speed U. Since the pressure has a definite limit, it also means that the bearing load capacity has also a limit, i.e. an ultimate value. In this regard, gas film bearings do show a significant difference with incompressible fluid (mineral oil lubricated) bearings whose (theoretical) load capacity increases with surface speed.

Closed form solutions for finite speed numbers (Λ) are not readily available. Hence, predictions of bearing film pressure and its force reaction supporting an applied load must rely on numerical analysis. For low to moderate speed numbers, finite differences or finite element methods applicable to elliptical differential equations are quite adequate. However, it is well known that these numerical methods are inaccurate and numerically unstable for large speed numbers (Λ) since the nature of the Reynolds equation evolves from a (second order) elliptical form into a (first order) parabolic form. See Ref. [8] for a significant advance that resolves the issue of pressure oscillations and numerical instability for large speed numbers (Λ)

Simple slider gas bearings

Consider, as shown in Figure 3, three typical one-dimensional[4] slider bearing configurations: tapered, Rayleigh-step, and tapered-flat. In these configurations, the width (B) >> length (L), and thus the hydrodynamic pressure does not vary along the z-axis. The bearing peak pressure and maximum load capacity are a function of the ratio between the inlet film thickness (h_1) and the exit film thickness (h_2) and the extent of the step or tapered length (L_1). Integration of the pressure field over the bearing surface gives the reaction load that opposes the applied load (W)

$$W = B\int_0^L (p - p_a)\,dx \quad \text{or} \quad w = \frac{W}{B\,L\,p_a} = \int_0^1 (P-1)\,d\bar{x} \tag{9}$$

[4] In this case, the bearing width (B) is much longer than its length (L); and hence the film pressure is only a function of the coordinate (x). The analysis calls for $\partial P/\partial z \ll \partial P/\partial x$.

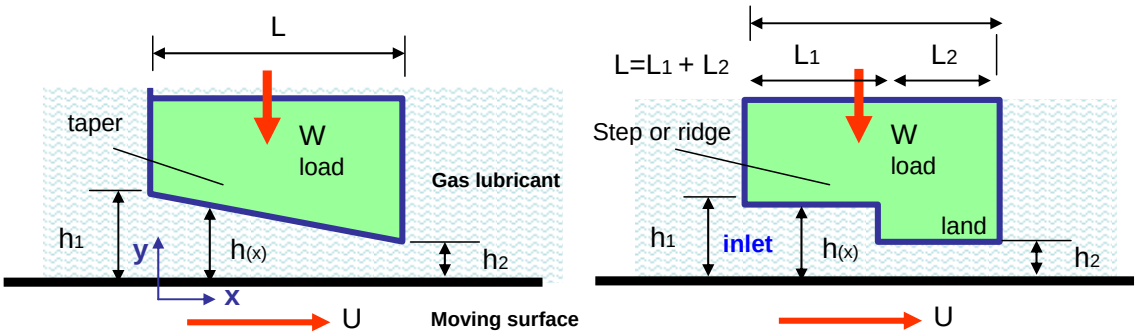

(a) Tapered bearing **(b) Rayleigh step bearing**

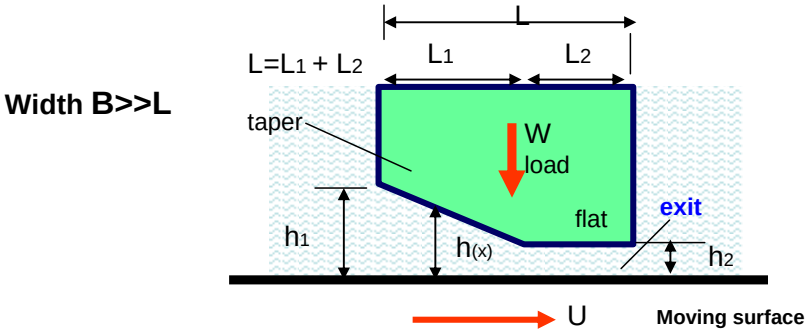

(b) Taper-flat bearing

Fig. 3 Schematic view of (simple) one-dimensional slider bearings

For small speed numbers $\Lambda<1$ (incompressible fluid), Table 2 shows closed-form expressions for the peak hydrodynamic pressure and the bearing reaction force (load) as a function of the film thickness ratio $\alpha = h_1/h_2$ and the land to length ratio $\gamma = L_2/L$ in a Rayleigh step bearing [22]. Simple calculations show that the maximum load $\bar{w}_{\max}$ requires of thickness ratios on the order of two, i.e., α=2.189 for a tapered bearing ($\bar{w}$ =0.0267), and α=1.843 for a step bearing with γ=0.30 ($\bar{w}$ =0.034). Hence, the taper height difference or the step height (h_1-h_2) is of similar size as the minimum film thickness (h_2). In gas bearings, the smallness of the film thickness required to support realistic loads also poses a difficulty in manufacturing mechanical features such as ridges and steps. Furthermore, manufacturing processes must ensure a surface roughness (RMS value) at least one order of magnitude (~1/10) lower than the minimum film thickness [21].

Table 2. Closed form expressions for peak hydrodynamic pressure and load in one dimensional tapered bearing and Rayleigh step bearing. Low speed operation (incompressible fluid approximation) $\Lambda = \left(6\,\mu U\,L \big/ p_a\, h_2^2 \right) < 1$. **[22]**

	$\alpha = h_1 \big/ h_2\,,\ \gamma = L_2 \big/ L$	**Tapered bearing**	**Step bearing**
Peak pressure	$\bar{p} = \dfrac{(p - p_a) h_2^2}{6\,\mu U\,L}$	$\dfrac{(\alpha - 1)}{4\alpha(1+\alpha)}$	$\dfrac{(\alpha-1)\gamma}{1 + \dfrac{\gamma\,\alpha^3}{1-\gamma}}$
Load	$\bar{w} = \dfrac{W\,h_2^2}{6\,\mu U\,B\,L^2}$	$\dfrac{1}{(1-\alpha)^2}\left[\ln(\alpha) + 2\dfrac{(1-\alpha)}{(1+\alpha)} \right]$	$\dfrac{\gamma}{2}\dfrac{(\alpha-1)}{1 + \dfrac{\gamma\,\alpha^3}{1-\gamma}}$

An example of gas bearing performance follows. Predictions are obtained for a film thickness ratio $\alpha = h_1 \big/ h_2$ =2.2 and length ratio $\gamma = L_2 \big/ L$ =0.30 for the Rayleigh-step and tapered flat bearings. The parameters used are close to those delivering a maximum reaction force (load capacity) in an incompressible lubricant slider bearing.

For increasing speed numbers (Λ), Figure 4 depicts the evolution of the hydrodynamic pressure field versus the coordinate (*x/L).* Note that the peak pressure displaces towards the minimum film location as Λ increases. Most important is to realize that the peak pressure, see Fig. 5, is <u>not</u> proportional to the speed, as is the case in incompressible lubricant bearings. The largest peak pressure cannot exceed that of the limit at high speeds, i.e., $p_{\max_{\Lambda\to\infty}} = \alpha = h_1/h_2$. This feature may entice designers to implement or promote high aspect ratios for the film thicknesses, $\alpha >> 1$. However; too large inlet/exit film ratios ($\alpha >> 1$) will cause the gas flow to choke at the bearing exit plane. This is an undesirable operating condition that produces noise and shock wave instabilities and could cause severe mechanical damage [2].

Figure 6 depicts the (dimensionless) load ($w=W/BLp_a$) versus speed number (Λ) for the three slider bearings. Note that at low speeds, $\Lambda < 5$ typically, the load capacity is proportional to the speed number. However, as Λ increases, the load reaches an asymptotic value. It is important to

note that knowledge derived from incompressible lubrication theory does not extend to gas lubrication theory. For example, the selected Rayleigh-step configuration offers the largest load at small speed numbers, i.e. in the incompressible fluid flow region. However, as evidenced in the predictions, at the highest speed numbers (Λ>100), the Rayleigh-step bearing produces the smallest load albeit it shows the largest peak pressure. Note that, see Fig. 4, in the step bearing the region of pressure generation is confined to the film land with small thickness (h_2); while the rest of the bearing is basically at ambient pressure.

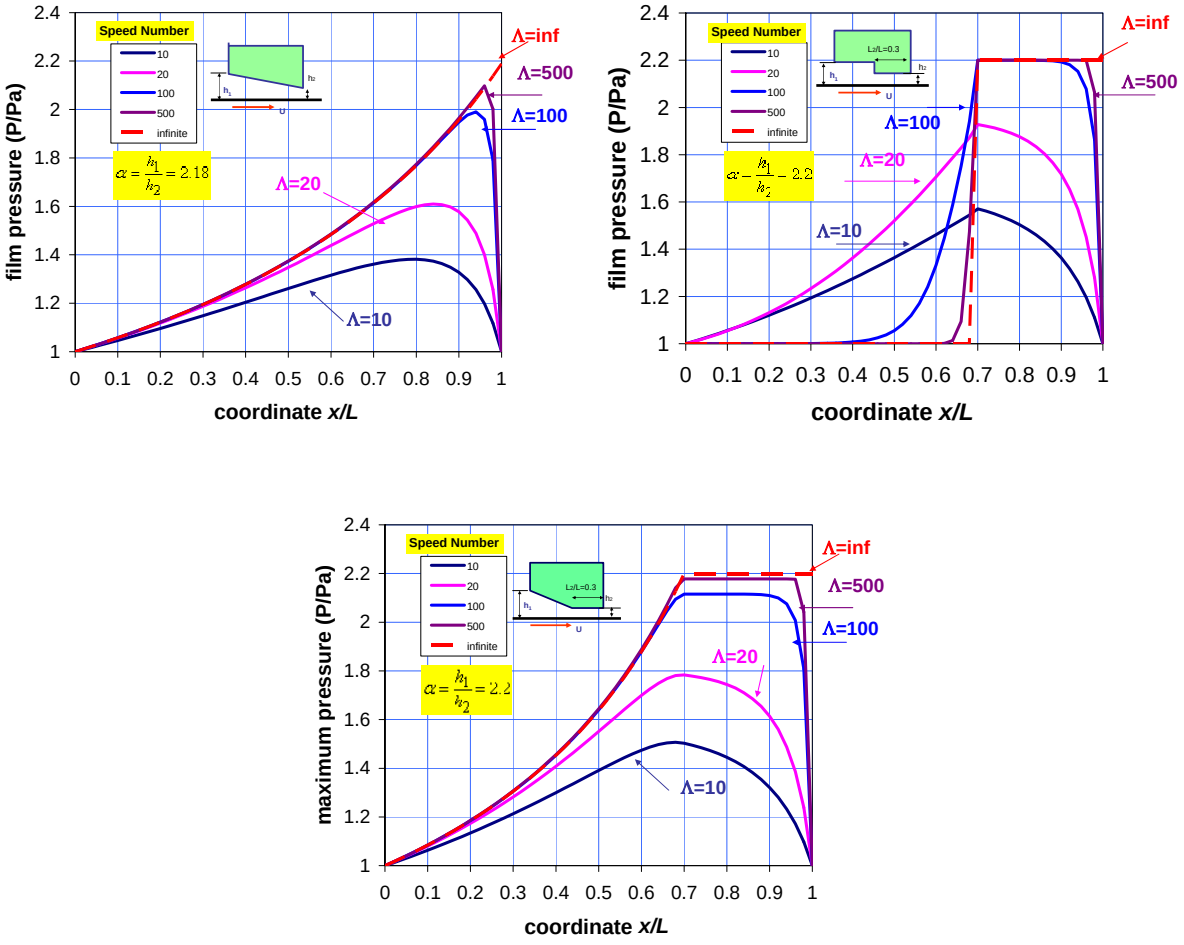

Fig. 4 Pressure field in one-dimensional slider bearings (tapered, Rayleigh step and tapered-flat) for increasing speed numbers (α=2.2, γ=0.3)

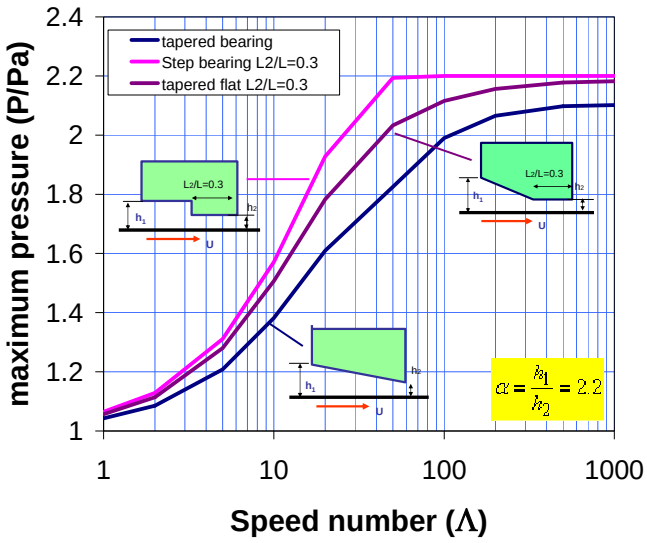

Fig. 5 Maximum film pressure in one-dimensional slider gas bearings versus speed number (Λ) (α = 2.2, γ = 0.3)

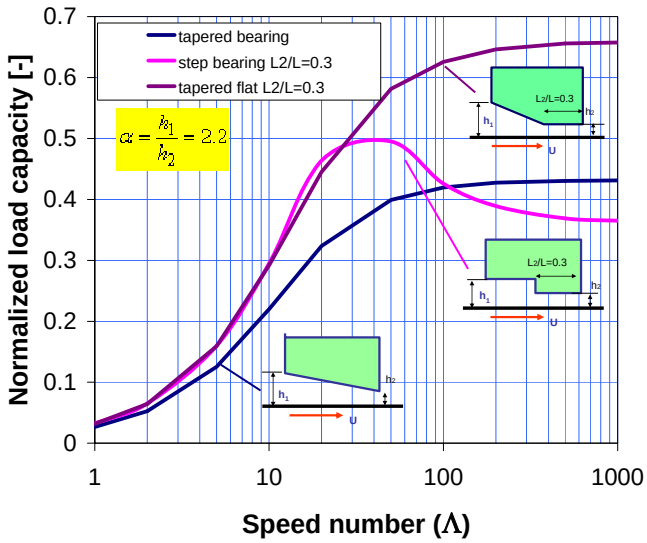

Fig. 6 Load capacity (*w*) in one-dimensional slider gas bearings versus speed number (Λ) (α = 2.2, γ = 0.3)

Dynamic force coefficients for slider gas bearings

Fluid film bearings support both static and dynamic loads. Thus far, the analysis has focused on the static load capacity. Consider a bearing that undergoes motions of small amplitude (Δy) and frequency (ω) about an equilibrium condition with film thickness $h_o(x)$. This equilibrium

film thickness renders a static reaction load balancing the external applied load (W_o). The (dimensionless) film thickness adds the static and dynamic components as[5]

$$H = H_o + \Delta H\, e^{i\tau};\ \Delta H = \Delta y \Big/ h_* \tag{10}$$

and the film pressure equals the superposition of the equilibrium pressure (P_o) and a perturbed, dynamic or first-order pressure field (P_1),

$$P = P_o + P_1\, \Delta H\, e^{i\tau} \tag{11}$$

Substitution of Eqs. (10-11) into Reynolds equation (3) gives, to first-order effects[6],

$$\frac{\partial}{\partial \bar{x}}\left(-\Lambda\, P_o\, H_o + \frac{H_o^3}{2}\frac{\partial\, P_o^2}{\partial \bar{x}} \right) = 0 \tag{12}$$

$$\frac{\partial}{\partial \bar{x}}\left(-\Lambda\, P_1\, H_o + \frac{H_o^3}{2}\frac{\partial (P_o\, P_1)}{\partial \bar{x}} \right) - i\,\sigma\, P_1\, H_o = -\frac{\partial}{\partial \bar{x}}\left(+\Lambda\, P_o + \frac{3H_o^2}{2}\frac{\partial \left(P_o^2\right)}{\partial \bar{x}} \right) + i\,\sigma\, P_o \tag{13}$$

The bearing reaction force equals

$$w = \int_0^1 (P_o - 1)\, d\bar{x} + \Delta H \left[\int_0^1 P_1\, d\bar{x} \right] e^{i\tau} \Rightarrow w_o + w_1\, \Delta H\, e^{i\tau} \tag{14}$$

The real and imaginary parts of w_1 give raise to the bearing stiffness (K) and damping (C) force coefficients, i.e.

$$Z = K + i\,\omega\, C = \frac{B\, L\, p_a}{\Delta y} \int_0^1 P_1\, d\bar{x} \tag{15}$$

In dimensionless form, the stiffness and damping coefficients become

$$\bar{K} = \frac{K}{B\, L\, p_a \Big/ h_*} = \mathrm{Re}\left(\int_0^1 P_1\, d\bar{x} \right);\ \ \bar{C} = \frac{C}{12\,\mu\, B \left(L_* \Big/ h_* \right)^3} = \frac{1}{\sigma}\,\mathrm{Im}\left(\int_0^1 P_1\, d\bar{x} \right) \tag{16}$$

Unlike bearings lubricated with incompressible fluids, the stiffness (K) and damping (C) force coefficients of gas bearings are strong functions of frequency [2, 4, 23]. In particular, for high speeds and high frequency operation ($\Lambda \to \infty, \sigma \to \infty$) $C \to 0$; i.e., damping is lost. Thus,

[5] See Lund [23] for the original and most elegant description of the analytical perturbation method for calculation of dynamic force coefficients in gas bearings.

[6] Products of first order terms are neglected, i.e. $P_1\, \Delta H^2 \sim 0$ for example.

gas bearings need to be used with great caution in applications that require mechanical energy dissipation to ameliorate or reduce vibrations of the mechanical system.

For the tapered-flat slider with $\alpha = h_1/h_2$ =2.2 and length ratio $\gamma = L_2/L$ =0.30, Figs. 7 and 8 depict the stiffness $\left(\bar{K}\right)$ and damping $\left(\bar{C}\right)$ coefficients versus increasing frequency numbers (σ) and various speed parameters (Λ) . Note two important dynamic force performance features: (a) the bearing stiffness rises rapidly with frequency, a typical hardening effect of gas bearings, and (b) damping decreases quickly, as expected[7]. It is also important to realize that, at low frequencies ($\sigma \sim 1$), the (nearly static) stiffness reaches a maximum at a certain speed (Λ>50), not increasing further with sliding speed. This is also expected since, as shown in Fig. 6, the load capacity also reaches its ultimate limit for operation at Λ>50.

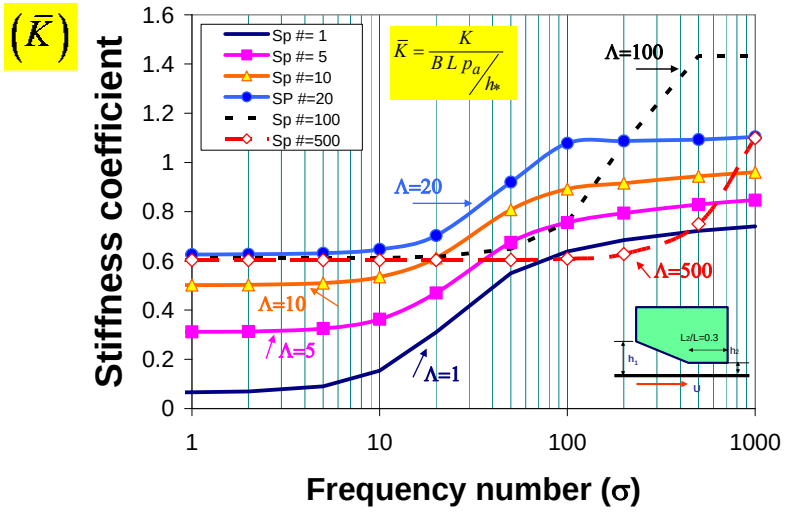

Fig. 7 Stiffness coefficient for 1D tapered-flat gas bearing versus frequency number (σ) and increasing speed numbers (Λ) (α = 2.2, γ = 0.3)

[7] Negative damping coefficients are not unusual in stepped gas bearings such as in spiral grooved or herringbone grooved configurations, see Ref. [7].

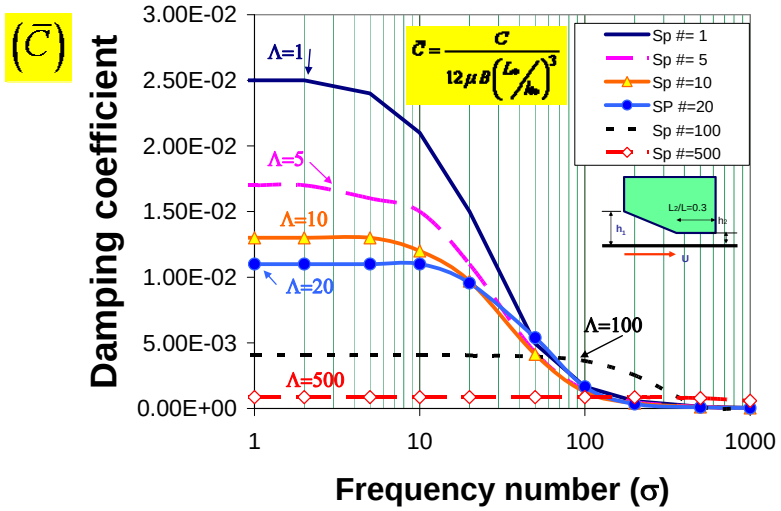

Fig. 8 Damping coefficient for 1D tapered-flat gas bearing versus frequency number (σ) and increasing speed numbers (Λ) (α = 2.2, γ = 0.3)

Cylindrical gas journal bearings

Cylindrical hydrodynamic bearings support radial (or lateral) loads in rotating machinery. Using gas as the lubricant in the fluid film bearing offers distinct advantages such as lesser number of parts, avoidance of mineral oils[8] with lesser contamination; and most importantly, little drag friction (minute power losses) and the ability to operate at extreme conditions in temperature, high or low, since gases are more chemically stable than liquids. On the other hand, gas bearings suffer from chronic problems including difficulties in their design and analysis, cost in manufacturing, and issues with installation and operation since bearing clearances are by necessity rather small.

Figure 9 shows three typical radial bearings of increasing mechanical complexity. The bearings portrayed are a cylindrical bearing (an idealized configuration), a multiple-pad bearing with hydrostatic pressurization, and a flexure-pivot bearing with hydrostatic pressurization. The external supply of pressure extends bearing life by aiding to promote an early lift off journal speed and reducing "hard landings" or transient rubs that lead to early wear of surfaces. In addition, hydrostatic pressurization enables the design and operation of gas bearings with

[8] Recall that liquid lubricated bearings may show cavitation, i.e. the hydrodynamic pressure cannot be lower than the liquid saturation pressure or that of the dissolved gases in the liquid. Gas bearings obviously do not show cavitation.

relatively large clearances, hence reducing their manufacturing costs and difficulties associated with their installation [10].

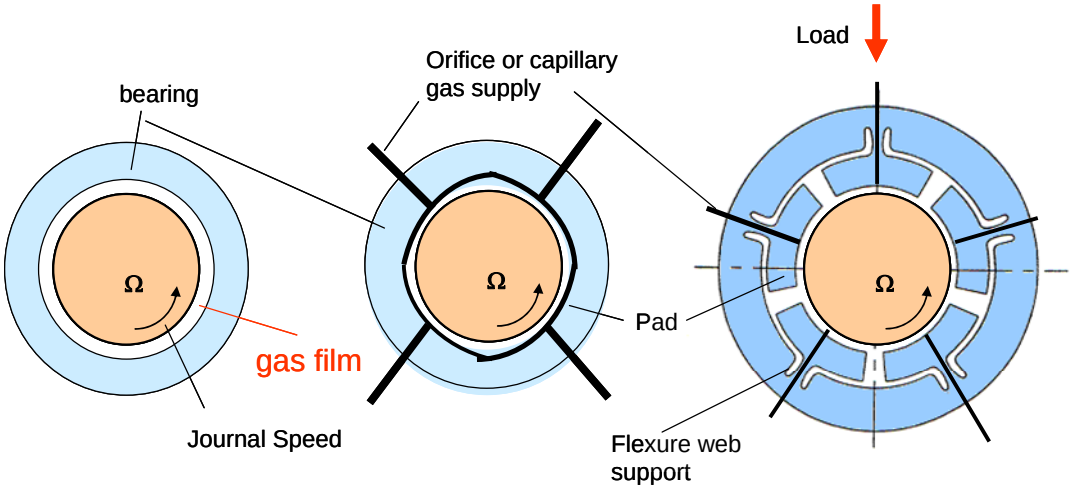

(a) Cylindrical journal bearing **(b) Multiple-pad bearing with holes for external pressurization** **(c) Flexure pivot – tilting pad bearing with holes for external pressurization**

Fig. 9 Cylindrical gas bearings – some typical configurations

External pressurization through restrictor ports also creates a centering stiffness and thus decreases the journal eccentricity needed for the bearing to support a load. A hybrid mode operation (combining hydrostatic and hydrodynamic effects) ultimately results in reduced power consumption. Disadvantages in gas bearings stem from two types of instabilities [2]: pneumatic hammer controlled by the flow versus pressure lag in the pressurized gas feeding system, and hydrodynamic instability, a self-excited motion characterized by sub synchronous (forward) whirl motions. Proper design of a hybrid bearing system minimizes these two kinds of instabilities[9]. Gas bearing design guidelines available since 1967 [24] dictate that, to avoid or delay a pneumatic hammer instability, externally pressurized gas bearings have restrictors impinging directly into the film lands, i.e. without any (deep) pockets or recesses.

The analysis herein does not discuss textured or etched bearings, i.e. ones with herringbone grooves, for example. See Ref. [7] for the appropriate analyses and predictions. The textured

[9] A self-excited instability means that a change in the equilibrium or initial state (position and/or velocity) of the RBS leads to a permanent departure with increasing amplitudes of motion at a certain frequency, usually a natural frequency. A self-excited instability does not rely on external forces (load condition), including mass imbalance, for its manifestation.

bearings are still costly to manufacture, offer little improvements in load capacity, and have severe limitations in terms of rotordynamic stability [12].

For certain static load dispositions, tilting pad bearings can eliminate the typically harmful hydrodynamic instability by not generating cross-coupled stiffness coefficients. Critical turbomachinery operating well above its critical speeds is customarily implemented with tilting pad bearings. The multiplicity of parameters associated with a tilting pad bearing demands complex analytical methods for predictions of force coefficients and stability calculations [10]. Incidentally, conventional (commercial) tilting pad bearings cannot be easily modified to add external pressurization (holes through pivots and pads) without constraining severely the pads' motion and adding sealing issues.

The flexure pivot – tilting pad bearing (FPTPB), see Fig. 9, offers a marked improvement over the conventional design since its wire discharge machining (EDM) construction renders an integral pads-bearing configuration, thus eliminating pivot wear and stack up of tolerances on assembly [13]. Each pad connects to the bearing through a thin flexural web, which provides a low rotational stiffness, thus ensuring small cross-coupled stiffness coefficients and avoiding subsynchronous instabilities into very high speed operation.

Thin film flow analysis for cylindrical bearings [10]

Figure 10 depicts the ideal cylindrical bearing with relevant nomenclature. The journal rotates at speed (Ω) and (e_X, e_Y) denote the journal displacements within the bearing clearance (c). The film thickness (h) around the bearing circumference is just

$$h = c + e_X \cos\Theta + e_Y \sin\Theta \tag{17}$$

Figure 11 depicts a schematic view of a flexure pivot tilting pad bearing. For operation with external pressurization, a feed orifice is machined through the thin web. A pad extends from Θ_l to Θ_t (leading and trailing edge angular coordinates) with three degrees of freedom corresponding to angular (tilt) rotation (δ_p), radial (ξ_p) and transverse displacements (η_p). The gas film thickness (h) in a pad is

$$h = c_p + e_X \cos\Theta + e_Y \sin\Theta + (\xi_p - r_p)\cos(\Theta - \Theta_p) + (\eta_p - R\delta_p)\sin(\Theta - \Theta_p) \tag{18a}$$

where c_P and r_p are the nominal machined clearance and pad preload at the offset Θ_P angle where the web is attached.

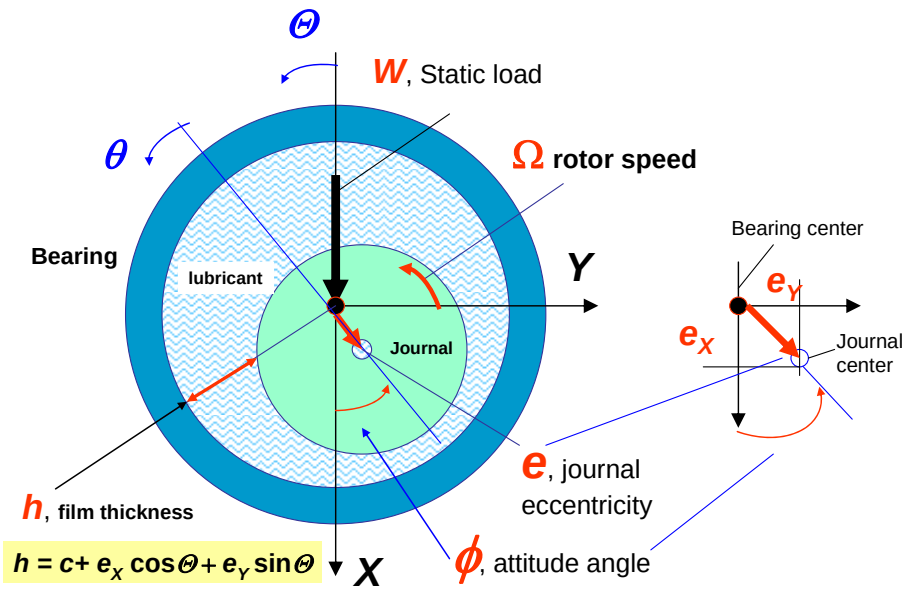

Fig. 10 Geometry of cylindrical gas bearing, coordinate system and nomenclature

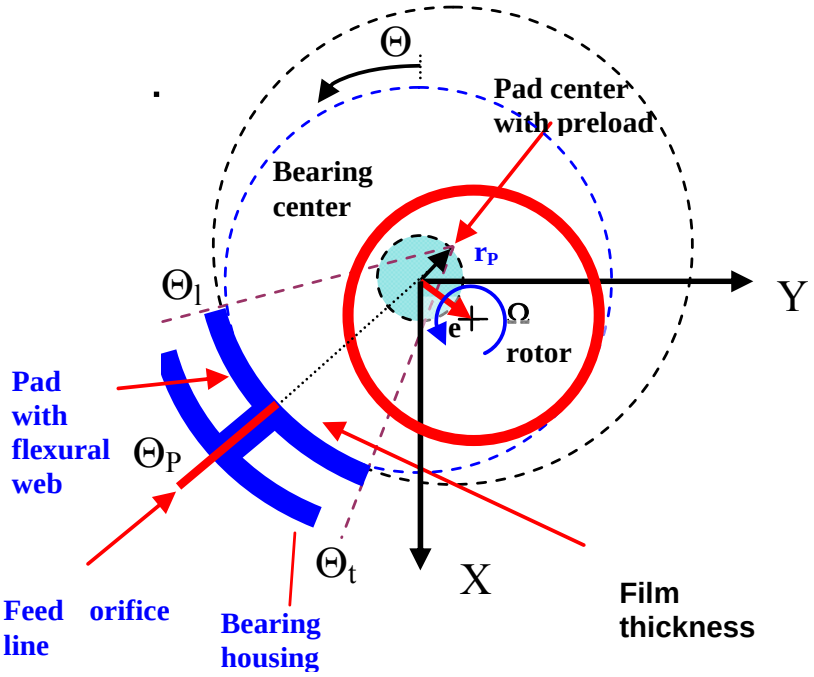

Fig. 11 Geometry of a flexure pivot pad bearing, coordinate system and nomenclature

Note that for a **rigid** pad with offset angle offset Θ_P and preload r_p, the film thickness simplifies to

$$h = c + r_p \cos\left(\Theta - \Theta_p\right) + e_X \cos\Theta + e_Y \sin\Theta \tag{18b}$$

In a radial bearing, Reynolds equation for the laminar flow of an ideal gas and under isothermal conditions governs the generation of hydrodynamic pressure within the thin film region, i.e., [2]

$$\vec{\nabla}\cdot\left(\frac{-h^3 p}{12\mu}\cdot\vec{\nabla}\,p\right) + \frac{\Omega}{2}\cdot\frac{\partial}{\partial\Theta}(p\,h) + \frac{\partial}{\partial t}(p\,h) = \sum \dot{m}_{OR}\left(\Re_g T\right) \tag{19}$$

where $\dot{m}_{OR}$ denotes mass flow through a supply port at pressure p_S. The pressure is ambient *(p_a)* on the sides (*z=0, L*) of a bearing pad.

For an inherent restrictor, the flow rate is a function of the pressure ratio $\bar{P} = p_{or}/p_S$, the orifice diameter (*d)* and the local film thickness (*h*), i.e. from [24],

$$\dot{m}_{OR} = \pi\, d\, h\, \frac{p_S}{\sqrt{\Re_g T}}\cdot\Phi(\bar{P}) \tag{20}$$

with
$$\Phi\left(\bar{P}\right) = \begin{cases} \left(2\cdot\dfrac{\kappa}{\kappa+1}\right)^{1/2}\cdot\left(\dfrac{2}{\kappa+1}\right)^{1/\kappa-1} & for \quad \bar{P} < \bar{P}_{choke} = \left(\dfrac{2}{\kappa+1}\right)^{\kappa/\kappa-1} \\ \left(2\cdot\dfrac{\kappa}{\kappa+1}\right)^{1/2}\cdot\bar{P}^{1/\kappa}\cdot\left(1-\bar{P}^{\kappa-1/\kappa}\right)^{1/2} & for \quad \bar{P} > \bar{P}_{choke} \end{cases} \tag{21}$$

where κ is the gas specific heats ratio. The orifice restriction is of *inherent type*[10] whose flow is strongly affected by the local film thickness.

An applied external static load (W_o) determines the journal center to displace eccentrically to the equilibrium position $(e_X, e_Y)_o$ with steady pressure field p_o and film thickness h_o, and corresponding pad deflections $(\delta_P,\ \xi_P,\ \eta_P)_{o,\ p=1,\ldots Npad}$.

As shown schematically in Fig. 12, let the journal center whirl with frequency ω and small amplitude motions $(\Delta e_X, \Delta e_Y)$ about the equilibrium position, The general motion of the journal center and the bearing pads[11] is expressed as,

[10] Externally pressurized gas bearings should not be manufactured with pockets or recesses to avoid pneumatic hammer effects, i.e. a self-excited instability characterized by sudden loss of damping even under static conditions (low frequencies) [24].

[11] For rigid cylindrical or multiple-pad bearings, the only displacements kept are those of the journal center $(\Delta e_X, \Delta e_Y)$; hence, the analysis is much simpler and straightforward.

$$e_X = e_{Xo} + \Delta e_X\, e^{i\omega t}, \qquad e_Y = e_{Yo} + \Delta e_Y\, e^{i\omega t},$$

$$\xi_p = \xi_{po} + \Delta\xi_p\, e^{i\omega t},\ \eta_p = \eta_{po} + \Delta\eta_p\, e^{i\omega t},\quad \delta_p = \delta_{po} + \Delta\delta_p\, e^{i\omega t} \qquad p = 1,2,\ldots,N_{pad} \qquad (22)$$

with $i = \sqrt{-1}$. The film thickness and hydrodynamic pressure are also given by the superposition of equilibrium (zeroth order) and perturbed (first-order) fields, i.e.

$$h = h_o + \Delta h\, e^{i\omega t} \qquad ; \qquad p = p_o + \Delta p\, e^{i\omega t} \qquad (23)$$

where

$$\Delta h = \Delta e_X \cos\Theta + \Delta e_Y \sin\Theta + \Delta\xi_P \cos(\Theta - \Theta_P) + (\Delta\eta_P - R\,\Delta\delta_P)\sin(\Theta - \Theta_P) \qquad (24)$$

and $$\Delta p = \left\{ p_X\, \Delta e_X + p_Y\, \Delta e_Y + p_\delta\, \Delta\delta_P + p_\xi\, \Delta\xi_P + p_\eta\, \Delta\eta_P \right\} \qquad (25)$$

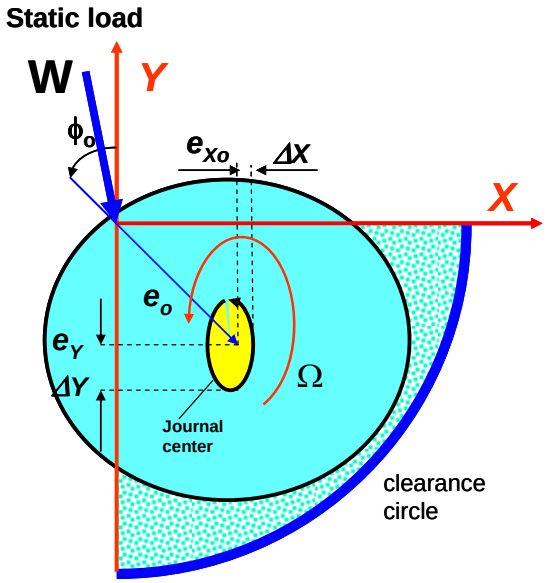

Fig. 12 Depiction of small amplitude journal motions about an equilibrium position

Substitution of Eqs. (24) and (25) into the Reynolds equation leads to a nonlinear PDE for the equilibrium pressure *(p_o)* and five linear PDEs for the first-order fields. For the equilibrium pressure p_o,

$$\frac{1}{R^2}\frac{\partial}{\partial\theta}\left(\frac{p_o\, h_o^3}{12\,\mu}\frac{\partial\, p_o}{\partial\theta}\right) + \frac{\partial}{\partial z}\left(\frac{p_o\, h_o^3}{12\,\mu}\frac{\partial p_o}{\partial z}\right) = \frac{\Omega}{2}\frac{\partial}{\partial\theta}(p_o\, h_o) \qquad (26)$$

See Ref. [10] for details on the first-order equations.

The external load vector with components (W_X, W_Y) acts on the journal. This load has a static part $(W_o, 0)$ and dynamic components $(\Delta W_X, \Delta W_Y)e^{i\omega t}$. The hydrodynamic pressure fields act on the rotor surface to produce reaction forces $\left(F_{P_X}, F_{P_Y}\right)$,

$$\begin{bmatrix} F_{P_X} \\ F_{P_Y} \end{bmatrix} = \int\int (p - p_a) \begin{bmatrix} \cos\Theta \\ \sin\Theta \end{bmatrix} R\, d\Theta\, dz \tag{27}$$

which balance the applied load, i.e.

$$\begin{aligned} W_X &= W_o + \Delta W_X\, e^{i\omega t} = -\sum_p F_{P_X}, \\ W_Y &= \qquad \Delta W_Y\, e^{i\omega t} = -\sum_p F_{P_Y} \end{aligned} \tag{28}$$

The film forces (with opposite sign) also act on each pad to induce a pitching moment (M_P),

$$M_P = R[\, F_{p_X} \sin\Theta_P - F_{p_Y} \cos\Theta_P \,] \tag{29}$$

Substitution of the pressure fields, zeroth and first order, into the pad force and moment equations leads to

$$\begin{Bmatrix} F_{P_X} \\ F_{P_Y} \\ M_P \end{Bmatrix} = \begin{Bmatrix} F_{P_{X_o}} \\ F_{P_{X_o}} \\ M_{P_o} \end{Bmatrix} - \begin{bmatrix} Z_{XX} & Z_{XY} & Z_{X\delta} & Z_{X\xi} & Z_{X\eta} \\ Z_{YY} & Z_{YX} & Z_{X\delta} & Z_{X\xi} & Z_{Y\eta} \\ Z_{\delta X} & Z_{\delta Y} & Z_{\delta\delta} & Z_{\delta\xi} & Z_{\delta\eta} \end{bmatrix} \begin{Bmatrix} \Delta e_X \\ \Delta e_Y \\ \Delta\delta_P \\ \Delta\xi_P \\ \Delta\eta_P \end{Bmatrix} e^{i\omega t} \tag{30}$$

where

$$Z_{\alpha\beta} = \{ K_{\alpha\beta} + i\omega\, C_{\alpha\beta} \}, \quad \alpha\beta = X, Y, \delta, \xi\, \eta \tag{31}$$

represent the gas film impedances acting on each pad, i.e. 25 stiffness (K) and damping (C) coefficients. The equations of motion for a pad with angular (δ_P), radial (ξ_P) and transverse (η_P) displacements are:

$$[M_P] \begin{Bmatrix} \ddot{\delta}_P \\ \ddot{\xi}_P \\ \ddot{\eta}_P \end{Bmatrix} + \left[K_P^S\right] \begin{Bmatrix} \delta_P \\ \xi_P \\ \eta_P \end{Bmatrix} + \left[C_P^S\right] \begin{Bmatrix} \dot{\delta}_P \\ \dot{\xi}_P \\ \dot{\eta}_P \end{Bmatrix} = \begin{Bmatrix} M_P \\ F_{P_\xi} \\ F_{P_\eta} \end{Bmatrix}$$

$$p=1,\ldots N_{pad} \tag{32}$$

$$\text{where } [M_P]=\begin{bmatrix} I_P & 0 & 0 \\ 0 & m_P & 0 \\ 0 & 0 & m_P \end{bmatrix},\ [K_P^S]=\begin{bmatrix} K_{\delta\delta}^S & K_{\delta\xi}^S & K_{\delta\eta}^S \\ K_{\xi\delta}^S & K_{\xi\xi}^S & K_{\xi\eta}^S \\ K_{\eta\delta}^S & K_{\eta\xi}^S & K_{\eta\eta}^S \end{bmatrix},\ [C_P^S]=\begin{bmatrix} C_{\delta\delta}^S & C_{\delta\xi}^S & C_{\delta\eta}^S \\ C_{\xi\delta}^S & C_{\xi\xi}^S & C_{\xi\eta}^S \\ C_{\eta\delta}^S & C_{\eta\xi}^S & C_{\eta\eta}^S \end{bmatrix} \quad (33)$$

are matrices representing the pad inertias, and the structural web stiffness and viscous damping coefficients, respectively.

Frequency reduced force coefficients for tilting pad bearings

Most analyses consider bearings as two degrees of freedom mechanical elements with lateral forces reacting to radial displacements (*x, y*). Bearing rotordynamic force coefficients are, by definition, changes in reaction forces due to small amplitude motions about an equilibrium position. The linearized model for a gas bearing is

$$\begin{Bmatrix} F_X \\ F_Y \end{Bmatrix} = -\begin{bmatrix} K_{XX} & K_{XY} \\ K_{YX} & K_{YY} \end{bmatrix}\begin{Bmatrix} x \\ y \end{Bmatrix} - \begin{bmatrix} C_{XX} & C_{XY} \\ C_{YX} & C_{YY} \end{bmatrix}\begin{Bmatrix} \dot{x} \\ \dot{y} \end{Bmatrix} = \mathbf{F} = -\mathbf{K}\,\mathbf{z} - \mathbf{C}\,\dot{\mathbf{z}} \quad (34)$$

where $\mathbf{F}=\{F_X,\ F_Y\}^T$ and $\mathbf{z}=\{x_{(t)}\ ,y_{(t)}\}^T$ are vectors of lateral reaction forces and displacements, respectively. Figure 13 shows a schematic idealized representation of the force coefficients as mechanical spring and viscous dashpot connections between the rotating journal and its bearing. Recall that gas bearings due to the fluid compressibility will show force coefficients that are strong functions of the excitation frequency. In tilting pad bearings, the complicated behavior is further compounded by the pads' radial and tilting motions.

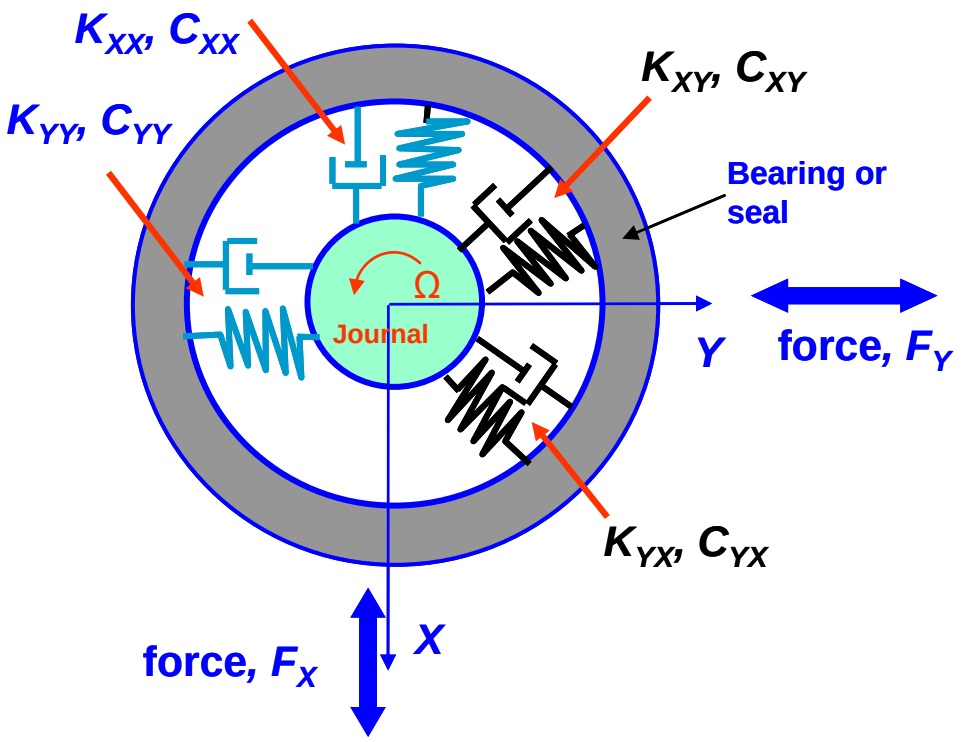

Fig. 13 Idealization of bearing force coefficients as viscous damping and stiffness elements

Clearly, in a tilting pad bearing the number of degrees of freedom equals = 2 (x, y) + 3 x N_{pad}. Hence, for example, a five pad bearing has 17 degrees of freedom. Clearly, the overabundance of degrees of freedom complicates the integration of bearing predictive tools into existing rotordynamic analyses. Hence, it is customary to reduce the bearing force coefficients by assuming that the pad motions are at the same frequency as the journal center lateral motions (X,Y). The set of frequency reduced impedance coefficients is [10]

$$[Z]_R = \begin{bmatrix} Z_{XX_R} & Z_{XY_R} \\ Z_{YX_R} & Z_{YY_R} \end{bmatrix} = [K]_R + i\,\omega [C]_R = \sum_P \left([Z_{XY}]_P - [Z_a]_P \left[Z_{p+f} \right]^{-1} [Z_b]_P \right) \quad (35)$$

The matrix $[Z]_R$ contains the frequency reduced stiffness and damping coefficients for rotor lateral motions (X,Y),

$$[K]_R = \begin{bmatrix} K_{XX_R} & K_{XY_R} \\ K_{YX_R} & K_{YY_R} \end{bmatrix}; [C]_R = \begin{bmatrix} C_{XX_R} & C_{XY_R} \\ C_{YX_R} & C_{YY_R} \end{bmatrix} \quad (36)$$

In the equation above,

$$[Z]_P = \begin{bmatrix} Z_{XX} & Z_{XY} & Z_{X\delta} & Z_{X\xi} & Z_{X\eta} \\ Z_{YX} & Z_{YY} & Z_{Y\delta} & Z_{Y\xi} & Z_{Y\eta} \\ Z_{\delta X} & Z_{\delta Y} & Z_{\delta\delta} & Z_{\delta\xi} & Z_{\delta\eta} \\ Z_{\xi X} & Z_{\xi Y} & Z_{\xi\delta} & Z_{\xi\xi} & Z_{\xi\eta} \\ Z_{\eta X} & Z_{\eta Y} & Z_{\eta\delta} & Z_{\eta\xi} & Z_{\eta\eta} \end{bmatrix}_P = \begin{bmatrix} [Z_{XY}]_{2x2} & [Z_a]_{2x3} \\ [Z_b]_{3x2} & [Z_c]_{3x3} \end{bmatrix}_P \qquad (37a)$$

and

$$[Z_{P+f}] = [K_P^S] + i\,\omega [C_P^S] + [Z_c] - \omega^2 [M_P] \qquad (37b)$$

is the composite (pad plus film) impedance matrix at frequency ω. For prediction of RBS imbalance responses, synchronous force coefficients are calculated with $\omega \equiv \Omega$. For eigenvalue RBS analysis, i.e. prediction of damped natural frequencies and damping ratios, iterative methods allow the determination of the coefficients at frequencies coinciding with the RBS natural frequencies.

As emphasized earlier, gas bearings (rigid surfaces, tilting pads and foil types) have frequency dependent force coefficients because of the fluid compressibility and the compliance of the bearing par surfaces. The dependency on frequency cannot be overlooked!

Some considerations on the solution of Reynolds equation for gas films

Most often the numerical solution of Reynolds equations (equilibrium and its variations for the dynamic first order pressure fields) is performed using algorithms suited for elliptical-type differential equations. Note also that Reynolds equation for the generation of gas film pressure is nonlinear due to the density varying with the pressure. In the case of a hydrostatic bearing carrying a static load, the equation becomes linear, i.e., Eq. (19) reduces to

$$\vec{\nabla} \cdot \left(\frac{-h^3}{24\mu} \cdot \vec{\nabla}\, p^2 \right) = 0 \qquad (38)$$

This equation can be solved efficiently for (p^2) as the independent variable with either central finite differences or finite element methods.

However, the more general bearing case that includes both hydrodynamic and hydrostatic effects remains nonlinear. In particular, one must realize that for large rotor speeds $(\Omega \to \infty)$ and/or large whirl frequencies $(\omega \to \infty)$, the character of the Reynolds equation

changes from elliptical to parabolic. Recall, in dimensionless form, that the compressible fluid film Reynolds equation is

$$\frac{\partial}{\partial \Theta}\left(PH^3 \frac{\partial P}{\partial \Theta} \right) + \frac{\partial}{\partial \bar{z}}\left(PH^3 \frac{\partial P}{\partial \bar{z}} \right) = \Lambda \frac{\partial}{\partial \Theta}(PH) + \sigma \frac{\partial}{\partial \tau}(PH) \tag{39}$$

where $$\Lambda = \frac{6\mu\Omega}{p_a}\left(\frac{R}{c}\right)^2 \text{ and } \sigma = \frac{12\mu\omega}{p_a}\left(\frac{R}{c}\right)^2 = \Lambda \frac{\omega}{\frac{1}{2}\Omega} \tag{4}$$

are the well-known speed and frequency numbers, respectively. At large speed numbers or frequency numbers $(\Lambda \gg 1, \sigma \gg 1)$, the first order terms on the right hand side dominate the generation of the hydrodynamic pressure in the gas film region. For low rotational speeds (Ω) and low frequencies, i.e., $(\Lambda, \sigma \to 0)$, the expansion $P \simeq 1 + \Lambda \bar{P}$ gives the linearized Reynolds equation

$$\frac{\partial}{\partial \Theta}\left(H^3 \frac{\partial P}{\partial \Theta} \right) + \frac{\partial}{\partial \bar{z}}\left(H^3 \frac{\partial P}{\partial \bar{z}} \right) = \frac{\partial H}{\partial \Theta} + \frac{\omega}{\frac{1}{2}\Omega}\frac{\partial H}{\partial \tau} \tag{40}$$

which is elliptical in character and formally identical to the Reynolds equation for an incompressible fluid. The numerical solution of the linear equation above can be easily performed using (central) finite differences, for example. More importantly, any predictive computational tool predicting pressure fields for bearings lubricated with incompressible fluids (oils) can also be used for gas films operating at low rotational speeds and/or low whirl frequencies. See Lecture Notes 7 for details on the numerical solution of Eq. (40)

For operation with large speeds, the *infinite speed* $(\Lambda \to \infty)$ equation for pressure generation is

$$0 = \frac{\partial}{\partial \Theta}(ph) \Rightarrow p = p_a \frac{h_a}{h(\Theta)} \tag{41}$$

which[12] establishes a limit on the generation of hydrodynamic pressure in a radial bearing. Consequently, the bearing reaction load will also reach a definite limit. The ultimate load capacity (w_u) of the cylindrical gas bearing is, as $\Lambda \to \infty$, [3]

[12] This solution is to be taken with caution since it does not satisfy all the boundary conditions, in particular at the bearing axial edges, i.e., $p = p_a$ at $z = \pm \frac{L}{2}$

$$w_u = \frac{W_{\max}}{p_a L D} = -\frac{(1+\varepsilon)}{2}\int_0^{2\pi} \frac{\cos\theta}{(1+\varepsilon\cos\theta)} d\theta = \frac{\pi(1+\varepsilon)\left[1-\left(1-\varepsilon^2\right)^{1/2}\right]}{\varepsilon\left(1-\varepsilon^2\right)^{1/2}} \qquad (42)$$

with the journal static eccentricity (ε=*e/c)* is along the direction of the applied load. Figure 14 shows that the ultimate load (w_u) grows modestly with journal eccentricity. Most importantly, the ultimate load is independent of the bearing clearance (c). The prospective user must realize that gas bearings, unlike liquid lubricated journal bearings, are not able to support heavy loads, as those typical in large rotating machinery[13]. The graph shows a recommended safe upper bound for load capacity selection at w_u=2 which renders an eccentricity (ε) ~0.60. Note that operation at any finite rotational speed will produce a higher shaft eccentricity. Furthermore, safe operation should avoid too large journal eccentricities that can provoke transient rubs and impacts that could quickly destroy the rotor bearing system.

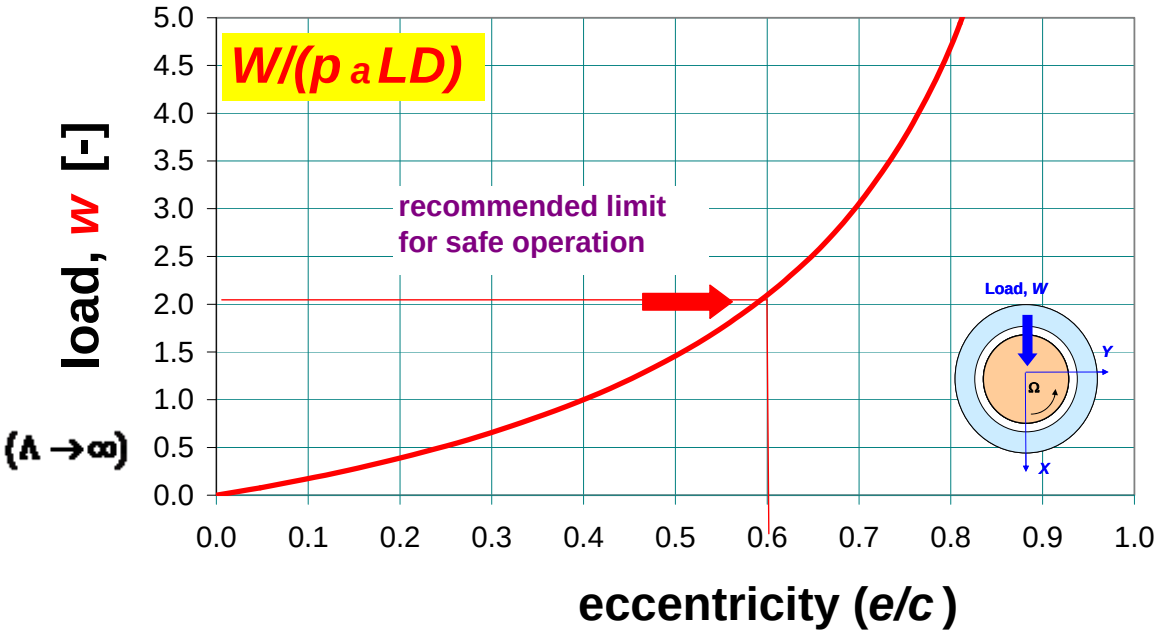

Fig 14. Ultimate load capacity (*W/p$_a$LD*) of cylindrical journal bearing. Infinite speed solution $(\Lambda \to \infty)$

[13] Specific load capacities $\left({}^{W}/_{p_a L D}\right)$ in oil bearings easily exceed 20 (bar) or more.

Incidentally, for operation with *infinite frequency* $(\sigma \to \infty)$, and for simplicity not accounting for shear flow effects $(\Lambda = 0)$, the squeeze film pressure is just

$$0 = \frac{\partial}{\partial \tau}(p\,h) \Rightarrow p \approx p_a \frac{h_a}{h(\Theta,\tau)} \tag{43}$$

Thus, the pressure is *in-phase* with the film thickness, i.e., solely determined by the displacements (e_X, e_Y) and not its time variations, i.e., not a function of the velocity at which the film thickness changes. These operating conditions thus lead to a stiffening or hardening of the gas film and absence of squeeze film damping effects. Examples showing this behavior were introduced for one-dimensional slider bearings.

Importantly enough, high frequency motions of a squeeze gas film can generate a mean pressure above ambient; and hence the ability to carry a static load (albeit small). See Ref. [2] for details on this rectification phenomenon.

Example of performance for a plain cylindrical journal bearing

Table 3 shows the geometry and operating conditions of a cylindrical journal bearing operating with air at ambient condition. The bearing application is typical for a miniature high speed spindle.

Table 3. Geometry and operating conditions of cylindrical gas bearing

Journal diameter, D	0.0285 m	L/D=1
Length, L	0.0285 m	
Clearance, c	0.020 mm	R/c=712
Lubricant: Air at 26.7 C		
Ambient pressure, p_a	1.01 bar	
Viscosity, μ	0.0185 c-Poise	
Density, ρ	1.16 kg/m^3	
Specific load, $p_a LD$	82 N	
Journal speed	10-100 krpm	Ω=RPM π/30
Load W	10 -100 N	

To show the bearing performance, define the following parameters:

$$w=\frac{W}{p_a L D}, \quad S=\frac{\mu N L D}{W}\left(\frac{R}{c}\right)^2, \qquad \Lambda=\frac{6\mu\Omega R L}{p_a c^2} \tag{44}$$

which represent the dimensionless load, Sommerfeld number and speed (or compressibility) number, respectively. Above N is the rotational speed in rev/s. Note that in the design (and selection) of a gas bearing the Sommerfeld number is (usually) known or serves to size the bearing clearance[14].

Figures 15 and 16 show the static (equilibrium) eccentricity (ε) and attitude angle (ϕ) versus Sommerfeld number (S). This angle is between the load vector and the ensuing journal eccentricity vector. Each graph includes the (unique) curve representative of the operation for the journal bearing with an incompressible lubricant. With an incompressible lubricant, large Sommerfeld numbers S , denoted by either a small load W, a high rotor speed Ω, or large lubricant viscosity μ, determine small operating journal eccentricities or nearly a centered operation, i.e. $\varepsilon \to 0$ and $\phi \to \frac{1}{2}\pi$ (90°). That is, the journal eccentricity vector **e** is nearly orthogonal or perpendicular to the applied load vector **W**.

A cylindrical (plain) gas bearing does not offer a unique performance curve; albeit the maximum journal eccentricity is bounded by the solution for the incompressible lubricant. The specific loads in a gas bearing are, by necessity, rather small. That is, even w=1.50 (see Fig. 15a) determines large operating eccentricities, in particular when the speed number (Λ) is also low.

As per the attitude angle (ϕ) , gas bearings show a smaller angle than with incompressible lubricants, in particular at high speeds, as evidenced by the predictions in Fig. 17 depicting ϕ versus the journal eccentricity.

[14] Even to this day, turbomachinery is designed (and built) with little attention to the needs of bearings and adequate lubrication for cooling and load support, static and dynamic. That is, thermo fluidic and aerodynamic considerations dictate the speed and size of the rotating elements. Fixed diameter and length for a bearing and the lubricant to be used, as well as the load to be supported, severely constrain the design space. The bearing designer has only the bearing clearance *(c)* to play with.

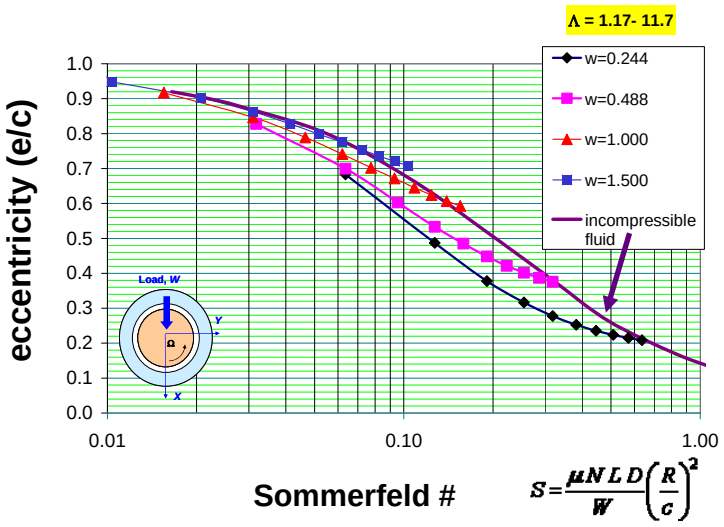

Fig. 15(a) Journal eccentricity vs. Sommerfeld # for cylindrical gas journal bearing. Load (*w*) increases

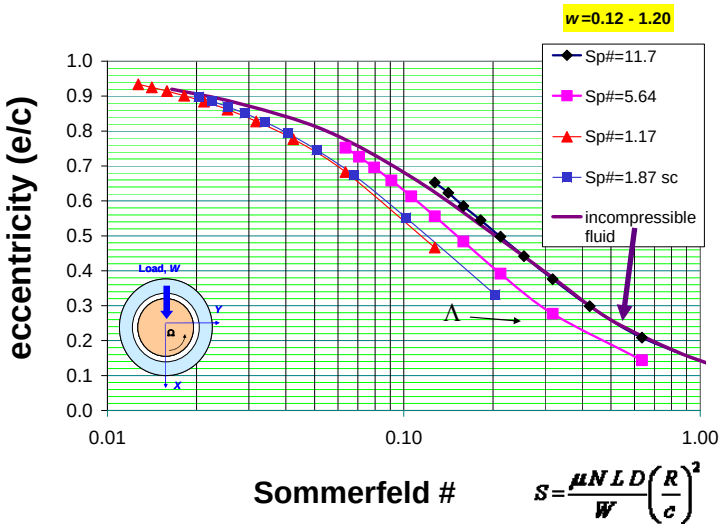

Fig. 15(b) Journal eccentricity vs. Sommerfeld # for cylindrical gas journal bearing. Speed # (Λ) increases

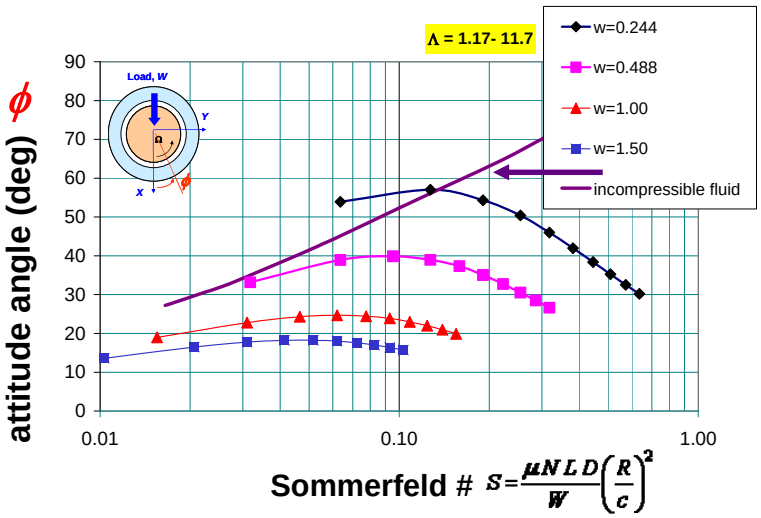

Fig. 16(a) Journal attitude angle vs. Sommerfeld # for cylindrical gas journal bearing. Load (*w*) increases

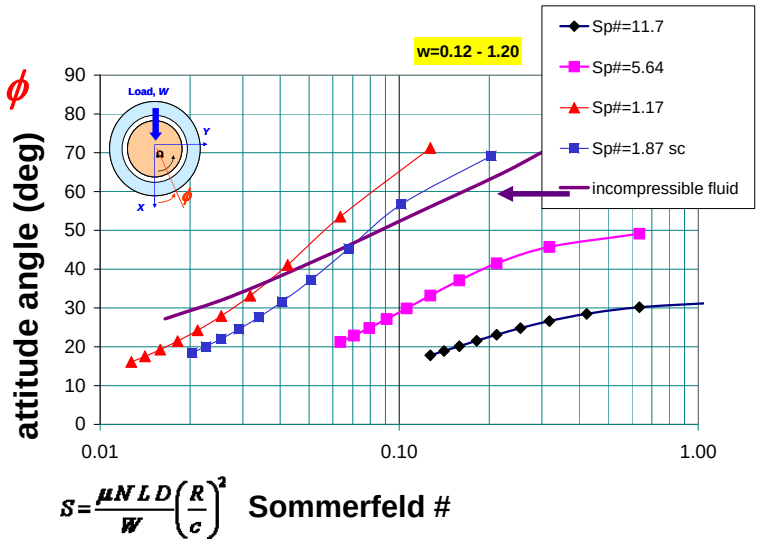

Fig. 16(b) Journal attitude angle vs. Sommerfeld # for cylindrical gas journal bearing. Speed # (Λ) increases

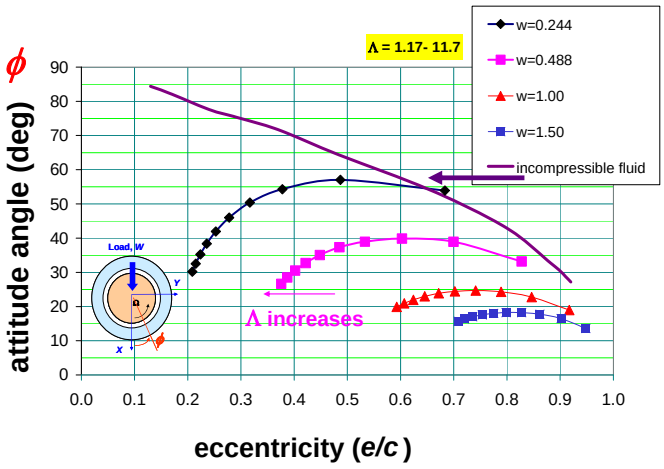

Fig. 17 Journal attitude angle vs. eccentricity for cylindrical gas journal bearing. Load (*w*) increases

Figure 18 shows the drag friction coefficient, $f = {T_{orque}}/{cW}$, is indistinguishable between incompressible fluid and gas film journal bearings. This is so since the shear stress model is viscous in character, i.e., not affected by fluid compressibility. The result does not mean a gas bearing has the same drag torque (and power loss $\wp = T_{orque}\,\Omega$) as a mineral oil bearing. The difference in viscosities causes the gas bearing to have a much lower drag coefficient; f is quite small, two orders of magnitude at least.

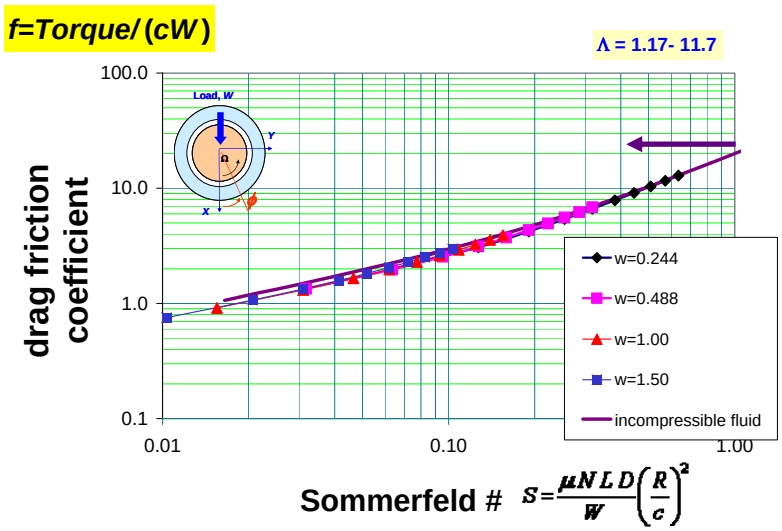

Fig. 18 Drag friction coefficient (*f*) vs. Sommerfeld number for cylindrical gas journal bearing. Load (*w*) increases

Bearing force coefficients and dynamic stability

Figure 19 depicts the bearing stiffness and damping force coefficients evaluated at a frequency coinciding with the journal rotational speed (ω=Ω). In the example, the dimensionless load w=0.488 while the journal speed increases from 10 krpm to 100 krpm. Hence, the bearing Speed number Λ=1.17 to 11.7, and the Sommerfeld number S=0.032 to 0.318. The dimensionless force coefficients are $\underline{K} = K \big/ (C_* \Omega)$, $\underline{C} = C \big/ C_*$; where $C_* = \mu \frac{D}{4}\left(\frac{L}{c}\right)^3$. See Fig. 15(a) for the relation between the journal eccentricity and the Sommerfeld number. Note that the direct stiffnesses ($\underline{K}_{XX}$, $\underline{K}_{YY}$) and damping ($\underline{C}_{XX}$, $\underline{C}_{YY}$) coefficients increase with the journal eccentricity (ε). At low eccentricities $(\varepsilon \to 0)$ or high speeds $(\Lambda \to \infty)$, i.e., $S \to 1$, then $\underline{K}_{XY}$=-$\underline{K}_{YX}$ and $\underline{C}_{XY}$=-$\underline{C}_{YX}$.

The stability of the rotor-bearing system is of interest. In general, this is an elaborate procedure that requires the integration of the fluid film bearing reaction forces into a rotordynamics model. Simple analyses consider a point mass (M) rigid rotor supported on a gas bearing. The (linearized) equations of motion of the system about an equilibrium conditions (**W=F)** are

$$M\begin{Bmatrix}\ddot{x}\\ \ddot{y}\end{Bmatrix}+\begin{bmatrix}K_{XX} & K_{XY}\\ K_{YX} & K_{YY}\end{bmatrix}\begin{Bmatrix}x\\ y\end{Bmatrix}-\begin{bmatrix}C_{XX} & C_{XY}\\ C_{YX} & C_{YY}\end{bmatrix}\begin{Bmatrix}\dot{x}\\ \dot{y}\end{Bmatrix}=\begin{Bmatrix}F_{X_e}\\ F_{Y_e}\end{Bmatrix} \tag{45}$$

$$\mathbf{M}\ddot{\mathbf{z}}+\mathbf{K}\mathbf{z}+\mathbf{C}\dot{\mathbf{z}}=\mathbf{F}_e$$

where $\mathbf{z}=\{x_{(t)}\ ,y_{(t)}\}^{\mathrm{T}}$ is the vector of dynamic displacements of the journal center. Above, $\mathbf{F_e}=\{F_X,F_Y\}^{\mathrm{T}}$ is the external dynamic force vector acting on the system, for example due to mass imbalance. The stability of the system considers the homogeneous form of Eq. (45) and assumes an initial state $(\mathbf{z_i}, \dot{\mathbf{z}}_\mathbf{i})$ away from the equilibrium condition (x=y=0).

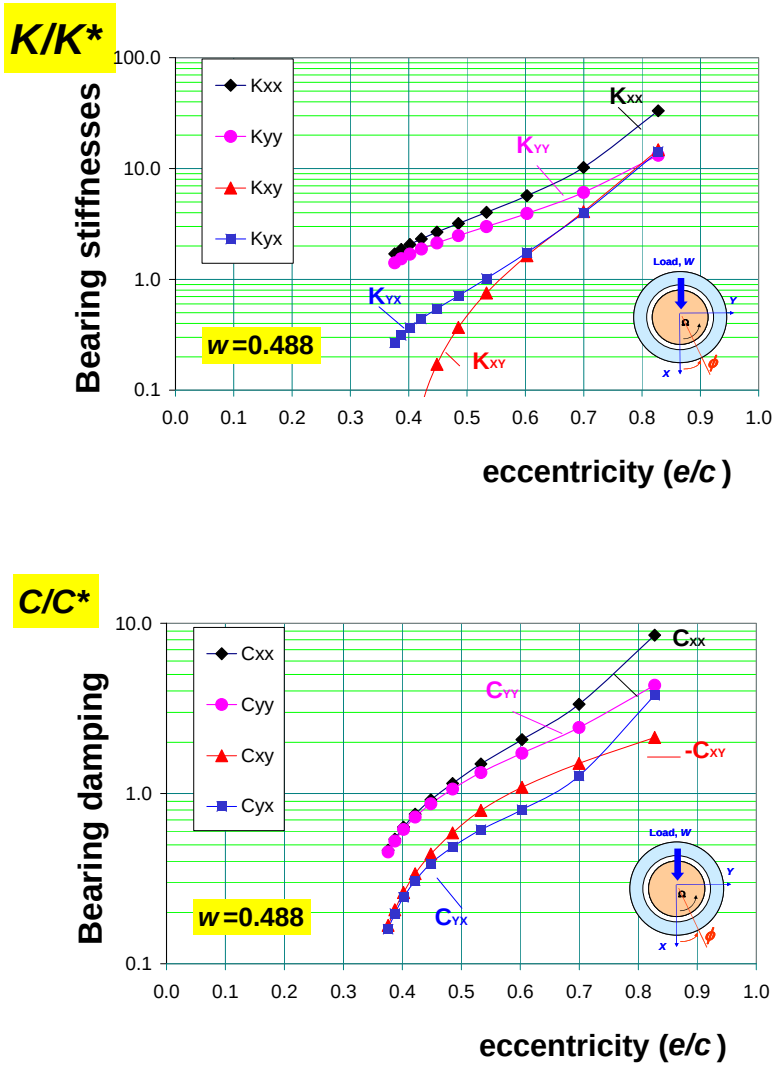

Fig. 19 Synchronous frequency stiffness and damping force coefficients vs. journal eccentricity for cylindrical gas bearing. Load *w*=0.488

The solution of the homogeneous form of Eq. (45) is straightforward. Let $\mathbf{z}=\mathbf{z_o}\, e^{st}$, hence Eq. (45) turns into the algebraic form

$$\left[\left(\mathbf{K}+s^2\mathbf{M}\right)+\mathbf{C}\,s\right]\mathbf{z}_o=\mathbf{0} \tag{46}$$

The roots of the characteristic equation $\left|\left(\mathbf{K}+s^2\mathbf{M}\right)+\mathbf{C}\,s\right|=0$ are $s_{1,2}=\lambda\pm i\,\varpi$. If the real part $\lambda < 0$, then the rotor bearing system (RBS) is stable; that is, a system that returns its equilibrium position, $\mathbf{z}\to\mathbf{0}$ as $t\to\infty$. If, on the other hand, $\lambda > 0$, then the RBS is unstable and $\mathbf{z}$

grows without bound[15]. At the threshold of instability, when $\lambda = 0$, the system will perform self-excited motions with whirl frequency ϖ, i.e. $\mathbf{z}=\mathbf{z_o}\, e^{i\,\varpi\, t}$. Hence, Eq. (46) becomes

$$\left[\ \mathbf{Z}-\varpi^2\,\mathbf{M}\ \right]\mathbf{z}_o=\mathbf{0}\ \text{ where }\ \mathbf{Z}=\left(\mathbf{K}+i\,\varpi\mathbf{C}\right) \tag{47}$$

Solution of Eq. (47) is straightforward for incompressible fluid, rigid surface, journal bearings since their force coefficients are frequency independent. The analysis leads to the estimation of the system critical mass (M_C) and the whirl frequency ratio (WFR) [25]

$$M_C\omega_S^2=K_{eq}=\frac{K_{XX}C_{YY}+K_{YY}C_{XX}-C_{YX}K_{XY}-C_{XY}K_{YX}}{C_{XX}+C_{YY}}$$

$$WFR^2=\left(\frac{\varpi_s}{\Omega}\right)^2=\frac{\left(K_{eq}-K_{XX}\right)\left(K_{eq}-K_{YY}\right)-K_{XY}\,K_{YX}}{C_{XX}\,C_{YY}-C_{XY}\,C_{YX}} \tag{48}$$

On the other hand, gas bearings have frequency dependent force coefficients, $\mathbf{K}_{(\omega)}$ and $\mathbf{C}_{(\omega)}$. As an example, for the particular operating conditions noted, Fig. 20 depicts the dimensionless stiffness $(\underline{K}_{ij})_{ij=X,Y}$ and damping $(\underline{C}_{ij})_{ij=X,Y}$ coefficients versus frequency ratio (ω/Ω) where Ω is the rotational speed; $\omega/\Omega=1$ denotes whirl frequency excitation synchronous with the rotational speed. Note that the direct stiffnesses increase with whirl frequency, a typical hardening effect due to fluid compressibility. On the other hand, the damping coefficients at high frequencies are zero, $\underline{C}_{ij}\to 0 \text{ as } \omega\to\infty$, also due to fluid compressibility. An iterative method is required to solve for the characteristic Eq. (47), $\left|\mathbf{Z}_{(\varpi)}-\varpi^2\,\mathbf{M}\right|=0$. Lund [24] restated Eq. (47) as $\mathbf{Z}_{(\varpi)}=\varpi^2\,\mathbf{M}$, and hence the instability threshold occurs at frequency ϖ_s where the imaginary part of the complex impedance Z_e is zero while its real part must be greater than zero. The equivalent impedance is

$$Z_{e_{(\varpi)}}=\frac{1}{2}\left(Z_{XX_{(\varpi)}}+Z_{YY_{(\varpi)}}\right)-\left[\ \tfrac{1}{4}\left(Z_{XX_{(\varpi)}}-Z_{YY_{(\varpi)}}\right)^2+Z_{XY_{(\varpi)}}Z_{YX_{(\varpi)}}\ \right]^2 \tag{49}$$

$$\text{Im}\left(Z_{e_{(\varpi_s)}}\right)=0 \text{ and } \text{Re}\left(Z_{e_{(\varpi_s)}}\right)>0 \tag{50}$$

The first statement above implies the effective damping is nil. For the data shown in Fig. 20, the RBS critical mass is just M_c=0.968 kg and the WFR=0.48. That is, for operation with journal

[15] It is a common misconception that the "no bound" statement implies system destruction. In actuality, the journal will whirl with a large amplitude whirl orbit bounded by the bearing clearance. As the motion amplitude grows, the bearing nonlinearity determines the size of the limit cycle. Of course, sustained operating under this condition is not recommended.

rotation at 50 krpm (833 Hz), the RBS becomes unstable if is physical mass is greater than M_c. If the actual system mass $M > M_c$, the RBS will begin self-excited motions at a frequency equaling 48% of the running speed, i.e. ϖ_s=400 Hz. This whirl frequency is also the natural frequency of the RBS for the noted operating condition. Czolczynski . For cylindrical gas bearings of various types Czolczynski [4] lists tables of rotordynamic force coefficients, critical mass and whirl ratios.

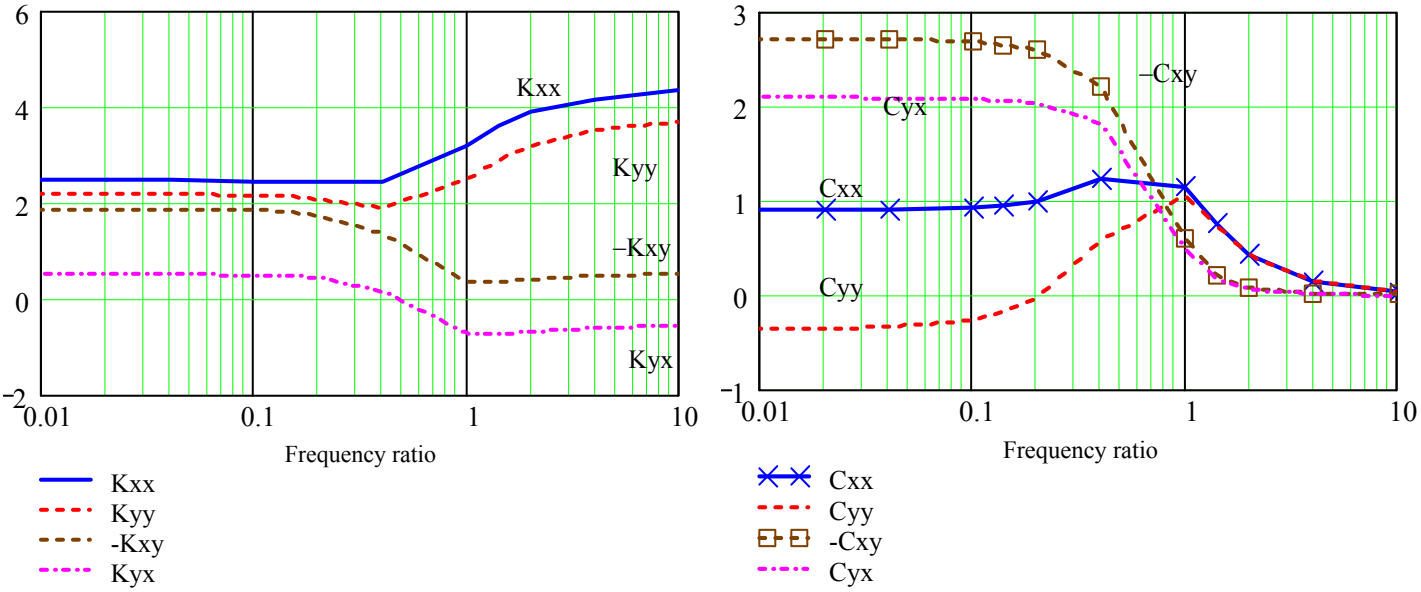

(a) stiffness coefficients, K (b) damping coefficients, C

Fig. 19 Bearing stiffness and damping force coefficients versus whirl frequency ratio (ω/Ω). Cylindrical gas bearing. Load *w*=0.488, speed = 50 krpm (Λ=5.843), S=0.158 (*e*/*c*=0.485)

Performance of a flexure pivot – tilting pad hydrostatic gas bearing

Cylindrical hydrodynamic journal bearings are notoriously limited in its load capacity as well as its dynamic stability. Hence, practice dictates the use of bearing configurations with multiple pads with a mechanical preload and, if possible, implementing hydrostatic pressurization to aid early rotor lift off as well as to reduce wear during start up and shut down events. As is well known in the rotating machinery industry, tilting pad bearings are preferred for high speed applications because of their excellent rotordynamic stability characteristics.

Figure 21 depicts a flexure pivot – tilting pad hydrostatic bearing that has undergone exhaustive investigation, analytical and experimental [13]. The test set up consists of a 190 mm rotor, weighing 0.827 kg, supported on a pair of gas bearings. Table 4 lists the geometry and operating conditions of the gas bearing installed for a load on pad condition. Note that the bearing pads have no pockets or recesses to eliminate pneumatic hammer effects. The gas feed orifices impinge directly on the rotor surface. In the application, the DN value= 2.9 million, where D and N = (journal diameter in mm) × (rotating speed in rpm). Note that the static load (W) on each bearing is low, typical of a high speed spindle motor or a small turbocharger, for example. Furthermore, compared to the journal bearing analyzed earlier, the current bearing clearance is larger for easiness in installation.

Table 4. Geometry and operating conditions of four pad flexure pivot, tilting pad hydrostatic bearing [13]

Journal diameter, D	0.0285 m	L/D=1.165
Length, L	0.0332 m	
Clearance, c	0.0375 mm	R/c=380
Preload, r/c	0.0071 mm	$r/c=0.20$
Pad arc length and pivot offset	72°	60%
Orifice diameter	0.62 mm	
Pad inertia and stiffness, I_P and $K_{\delta\delta}$	0.253 g-mm^2	20 Nm/rad
Lubricant: Air at 26.7 C	1.01 bar	Ambient pressure, p_a
Viscosity, μ	0.0185 c-Poise	
Density, ρ	1.16 kg/m^3	
Supply pressure, p_S	2.39, 3.77, 5.15 bar	
Load, W along X	4.05 N	$w=W/p_aLD$=0.042
Journal speed, Ω	10-100 krpm	Ω=RPM π/30

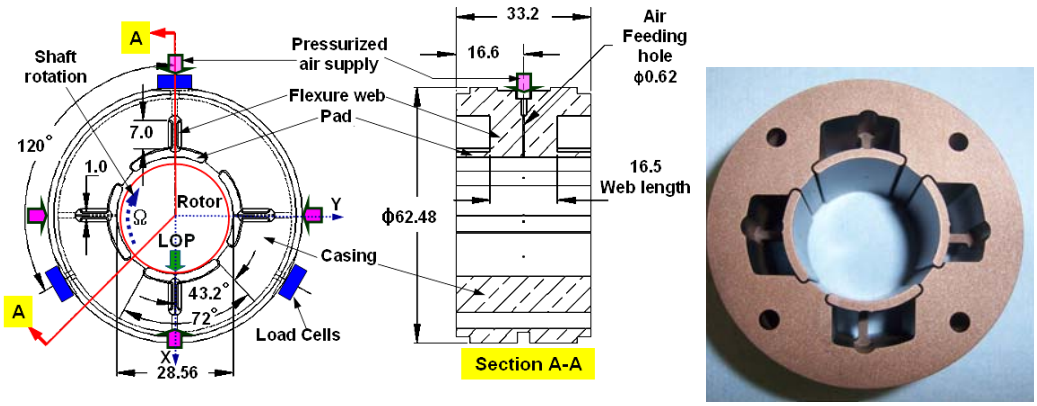

Fig. 21 Dimensions of flexure pivot hydrostatic gas bearing (units: mm) [13]

Figure 22 shows the bearing static eccentricity (ε), attitude angle (ϕ) and friction coefficient (f) versus speed number (Λ). The predictions are for speeds from 10 to 100 krpm, Λ=0.81−8.11 with S=0.234-2.346, with hydrodynamic operation (no external pressurization) and hydrostatic pressurization with pressure supplies, p_S= 2.39, 3.77 and 5.15 bar (absolute) [20, 40, 60 psig]. External pressurization leads to small journal eccentricities (ε) and attitude angle (ϕ), with a minor reduction in friction coefficient (f). In particular, the highest supply pressure gives a nearly centered journal operation. Figure 23 shows the flow rate (g/s) versus pressure and comparisons with experimental data. The supplied flow is quite small (max. 14.7 LPM), easily bleed off from a compressor in an actual RBS without significant penalty in its efficiency.

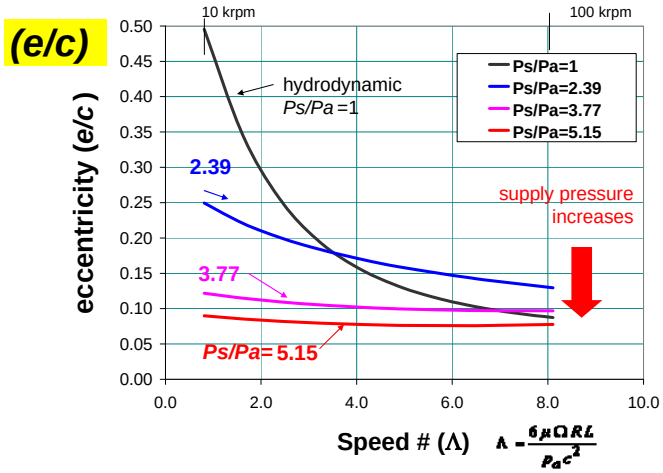

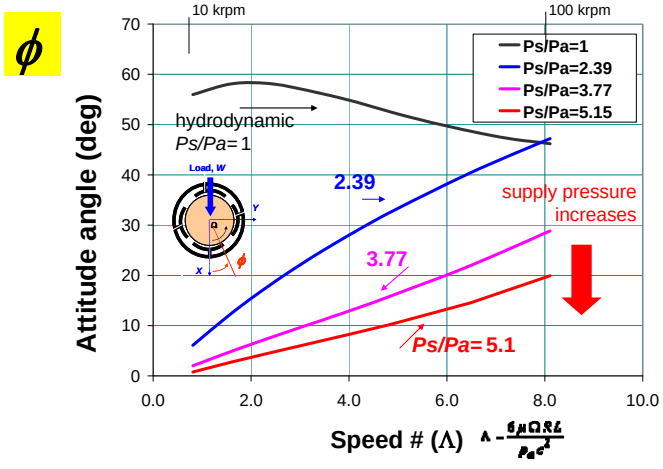

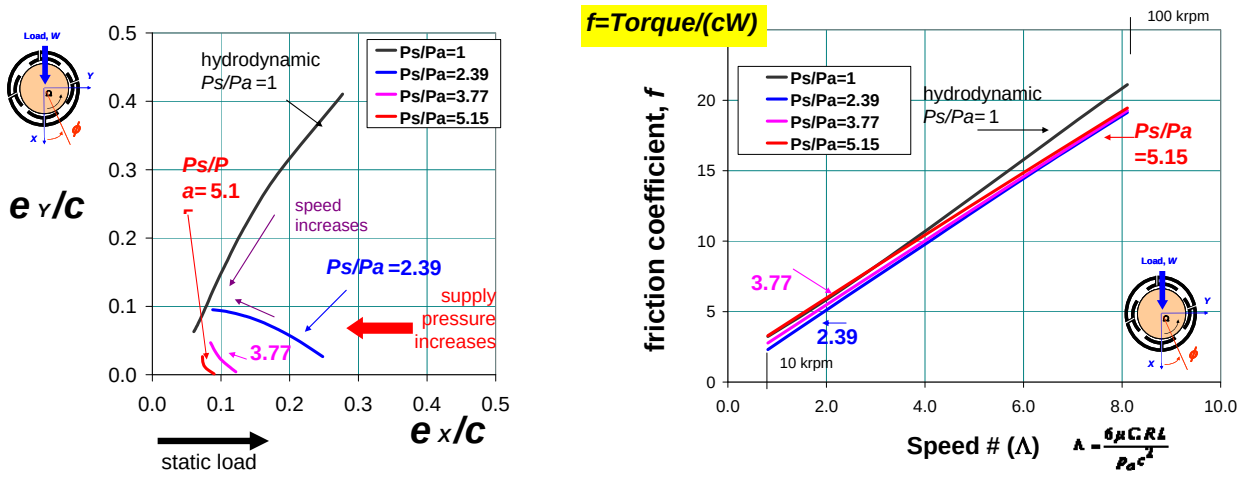

Fig. 22 Static performance of flexure pivot hydrostatic gas bearing versus speed (Λ): journal eccentricity *(e/c)*, attitude angle (*ϕ*), journal center locus e_Y vs. e_X, and friction coefficient (*f*) vs. Load (*w*) fixed

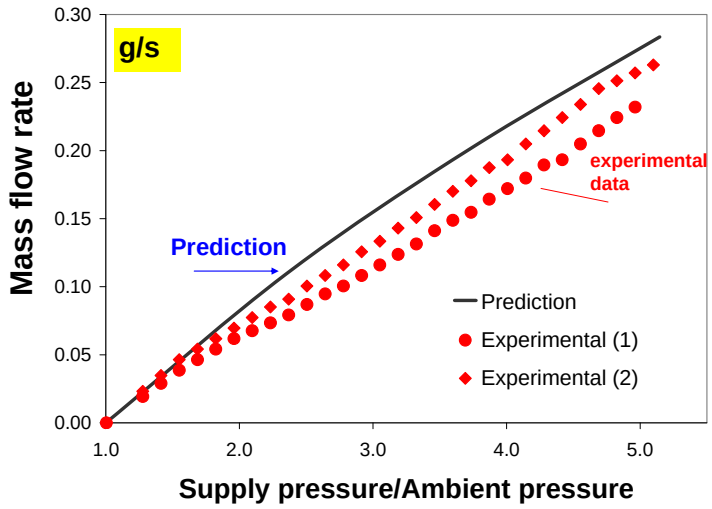

Fig. 23 Predicted and measured flow rate for flexure pivot hydrostatic gas bearing versus supply/ambient pressure ratio

Figure 24 depicts the (dimensionless) bearing force coefficients, synchronous speed reduced (ω=Ω), versus speed for increasing magnitudes of external pressurization. Note that the cross-coupled stiffnesses ($\underline{K}_{XY}$, $\underline{K}_{YX}$) are a small fraction of the direct stiffnesses ($\underline{K}_{XX}$, $\underline{K}_{YY}$), these growing with the level of supply pressure. The direct damping coefficients ($\underline{C}_{XX}$, $\underline{C}_{YY}$), on the

other hand, decrease rapidly with an increasing pressure supply and less steeply with journal speed.

The drop in damping as speed increases is a typical effect of fluid compressibility. The sharp reduction in damping with pressurization is problematic since, with the increase in bearing direct stiffness, it will produce a significant reduction in system damping ratio. Nonetheless, the model predicts the bearing will have a low whirl frequency ratio (WFR)~0.15, a significant improvement over the conventional cylindrical journal bearing.

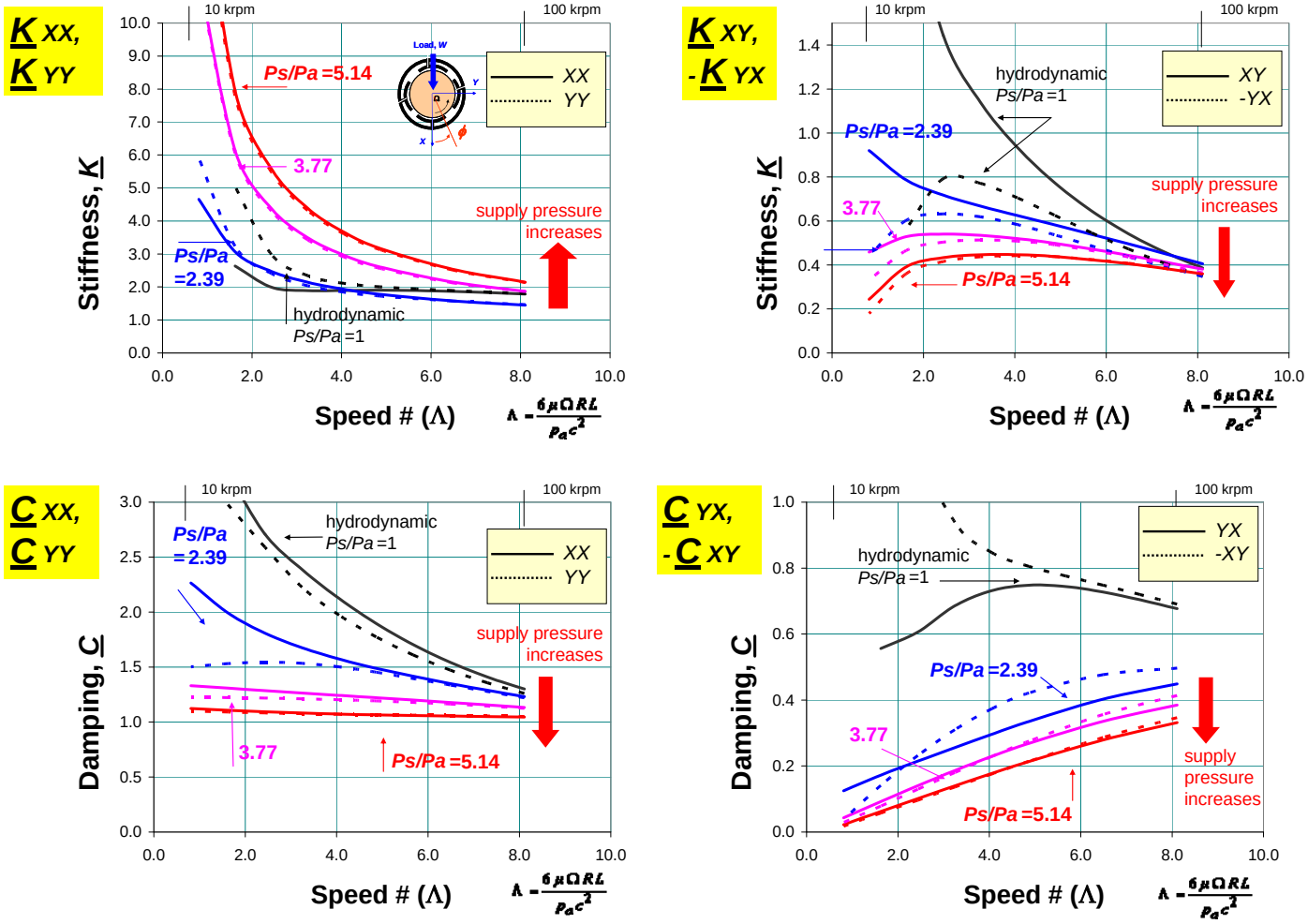

Fig. 24 Stiffness (*K*) and damping (*C*) coefficients of flexure pivot hydrostatic gas bearing versus speed (Λ). Synchronous speed force coefficients. Load (*w*) fixed

Figure 25 shows the predicted and measured synchronous rotor imbalance response for operation with 2.36 bar and 5.08 bar (ab) feed pressure into the bearings. Note the effect of

supply pressure on increasing the system critical speed as well as in reducing the damping ratio. See Refs. [26,27] for further details on the experimental investigation which includes tests with external loads to determine the reliability of the gas bearings under intermittent shocks and periodic forces simulating maneuver loads and uneven road conditions. Furthermore, the test data in the figure suggests the possibility of controlling the supply pressure to move critical speeds and avoid the passage through resonances. Ref. [13] discusses and implements a simple and inexpensive control strategy that demonstrated remarkable results. In brief, external pressurization is only needed at low rotor speeds, while at high rotor speeds it can be safely dispensed with.

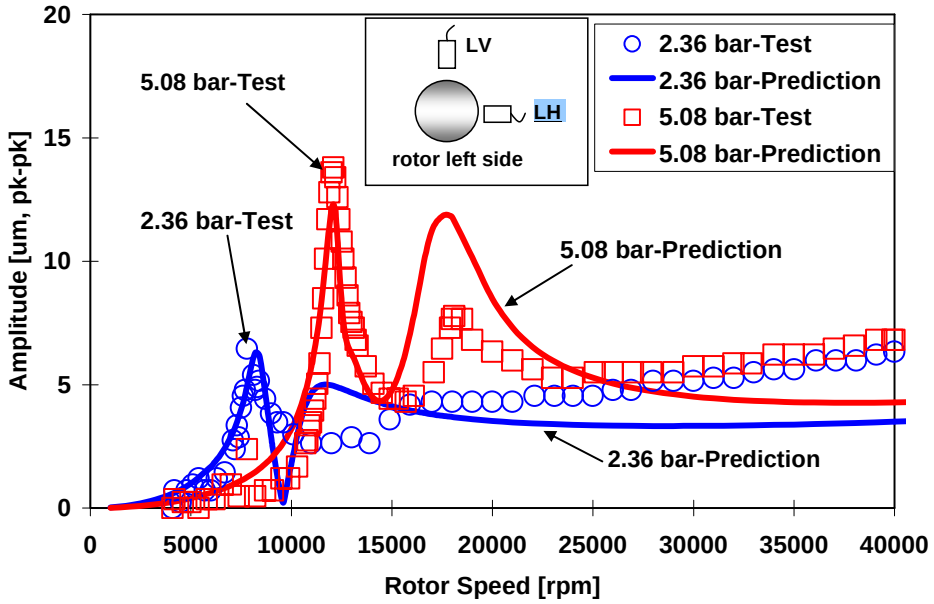

Fig. 25 Comparison of predicted and measured imbalance response of rotor supported on flexure pivot hydrostatic gas bearings. Operation with p_S= 2.36 bar and 5.08 bar (abs) supply pressure [26].

An introduction to gas foil bearings

Oil-free systems have a reduced part count, footprint and weight and are environmentally friendly with demonstrated savings in long-interval maintenance expenses. Until recently, gas bearings were constructed with hard or rigid surfaces to reduce friction during start up or shut down events. However, bearing types such as herringbone groove bearings require tight

clearances (film thicknesses), and with their hard surfaces offer few advantages for use in high speed MTM.

Gas foil bearings (GFBs) have emerged as a most efficient alternative for load support in high speed machinery. These bearings are compliant surface hydrodynamic bearings using ambient air as the working fluid media. Recall Fig. 1 showing two typical GFB configurations, one is a multiple overleaf bearing and the other is a corrugated bump bearing. Both bearing types are used in commercial rotating machinery, yet the open literature presents more details on bump-GFBs, along with measurements and analyses. The corrugated bump foil bearing is constructed from one or more layers of corrugated thin metal strips and a top foil. In operation, a minute gas film wedge develops between the spinning rotor and top foil. The bump-strip layers are an elastic support with engineered stiffness and damping characteristics [5,18].

GFBs offer distinct advantages over rolling elements bearings including no DN[16] value limit, reliable high temperature operation, and large tolerance to debris and rotor motions, including temporary rubbing and misalignment, Current commercial applications include auxiliary power units, cryogenic turbo expanders and micro gas turbines. Envisioned or under development applications include automotive turbocharger and aircraft gas turbine engines for regional jets and helicopter rotorcraft systems [5]. Alas, GFBs have demerits of excessive power losses and wear of protective coatings during rotor startup and shutdown events. In addition, expensive developmental costs and, until recently, inadequate predictive tools limited the widespread deployment of GFBs into mid size gas turbines. In particular, at high temperature conditions, reliable operation of GFB supported rotor systems depends on adequate engineered thermal management and proven solid lubricants (coatings).

Successful implementation of GFBs in commercial rotating machinery involves a two-tier effort; that of developing bearing structural components and solid lubricant coatings to increase the bearing load capacity while reducing friction, and that of developing accurate performance prediction models anchored to dependable (non commercial) test data. Chen et al. [18] and DellaCorte et al. [5,28] publicize details on the design and construction of first generation foil bearings, radial and thrust types, aiming towards their wide adoption in industry.

[16] DN, the product of journal diameter (mm) times rotational speed [RPM], is a limiting factor for operation of rolling element bearings (DN= 2 Million in specialized bearings with ceramic balls, for example)

Performance of a simple one dimensional foil slider bearing

Figure 26 depicts a one dimensional tapered foil (bump strip) bearing. The dimensionless film thickness (H) and Reynolds equation for the hydrodynamic pressure (P) are:

$$H = H_R(\bar{x}) + S\,(P-1)\ ;$$

$$\bar{\nabla}\cdot\left(-H^3\,P\cdot\bar{\nabla}(P)\right) + \Lambda\cdot\frac{\partial}{\partial\bar{x}}(PH) + \sigma\frac{\partial}{\partial\tau}(PH) = 0 \qquad (51)$$

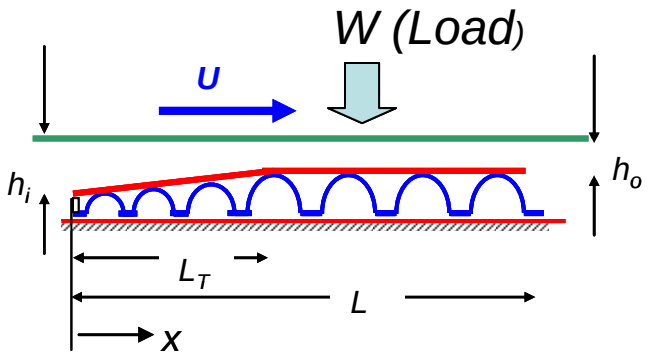

Fig. 26 Schematic view of tapered foil-bump strip bearing (width B)

where $\bar{x} = \frac{x}{L},\ \tau = \omega t, P = \frac{p}{p_a}, H = \frac{h}{h_*}\ \Lambda = \frac{6\mu U L}{p_a h_*^2},\ \sigma = \frac{12\,\mu\,\omega\,L^2}{p_a h_*^2},\ \underline{S} = \frac{\underline{s}\,p_a}{h_*}$ (52)

h_R is the film thickness for a rigid surface bearing and $\underline{s} = \frac{1}{k_b(1+i\gamma)}$ is the foil support compliance or flexibility coefficient[17], also accounting for material damping with a loss factor (γ). In most applications reported in the literature, the parameter ($\underline{S}$) does not exceed a magnitude equal to 5. Indeed, typical bump foil stiffnesses range from k_B = 5 to 100 (MN/m^2)/mm [18], and thus, operation at ambient conditions (p_a= 1 bar) with a film thickness of 5 micrometer leads to $\underline{S}$ varying from 0.2 to 4 for fixed end and free end bump-foil strips, respectively. Compliance ($\underline{S}$) magnitudes below 0.1 imply an almost rigid surface bearing; while $\underline{S}$> 5 correspond to a bearing too soft to support any practical load.

[17] The description is rather simplistic, it neglects the elastic forces of the top foil and assumes that only the local pressure deforms a bump. Realistic physical models are available, see Ref. [16] for example.

The most difficult issue in foil bearing design relates to the estimation of the actual film thickness separating the foil from the moving surface. The operating thickness is unknown since all foil bearings have zero clearance at the stationary condition, i.e. without surface speed. The issue is resolved in a simple and ingenious manner.

The applied (dimensionless) load on the bearing is $w = W / p_a L B$, where B is the bearing width. At static conditions, the surface speed is $U=0$ $(\Lambda = 0)$, and the bearing supports the load through the elastic deformation of the bump foil strip along the length $(L-L_T)$. The contact pressure is simply $p_c = \dfrac{W}{(L-L_T)B}; \left(P_c = \dfrac{w}{(1-l_T)} \right)$, which determines the largest deflection on the foil bump structure, $\delta_{U=0} = (p_c - p_a)/k_b$. Clearly, ($\delta$) should be within the elastic region of the elastic sub-structure (bump strip)[18]. Note that this simple condition dictates the choice of the foil stiffness within acceptable engineering practice.

Now consider the bearing operates at an exceedingly large surface speed, $U \to \infty (\Lambda \to \infty)$. This condition reduces Reynolds Eq. (51) to the (PH) limit, i.e.

$$\frac{\partial}{\partial \bar{x}}(PH) = 0 \;\Rightarrow PH = 1 \; H_i = P_o \left(H_R + S\left[P_o - 1\right] \right) = P_o H_o \qquad (53)$$

where (P_o, H_o) denotes the gas pressure and film thickness in the downstream section of the foil, and $H_i = H_T + H_o$ is the film thickness at the inlet section. This last equation is easily solved with the load constraint $w = \int_0^1 (p-1)\, dx$, to determine the film thickness H_o. Note that this ultimate film thickness is the largest ever to occur. Thus, actual operating conditions (with finite speed) must render a smaller film thickness.

Figure 27 shows the foil bearing ultimate load (w) decreases rapidly as the bearing compliance ($\underline{S}$) increases for two inlet film thickness (H_i=3, 6)[19]. Figure 28 displays the bump strip elastic deflection, and contact and lift pressures versus the bearing compliance $(\underline{S})$. Note that for operation at "infinite" speed the foil elastic deflection and lift pressure are smaller than for the contact condition since the hydrodynamic pressure distributes more evenly over the whole

[18] Other constraints also apply. Most notably those related to tip clearances on rotating wheels and on inter-stage seals within a typical turbomachinery.

[19] Even a rigid bearing ($\underline{S}$=0) does have an ultimate (speed limited) load capacity due to the gas compressibility. See prior sections.

bearing surface (see Fig. 29). At U=0, the contact zone conforms to the non-tapered portion of the bearing.

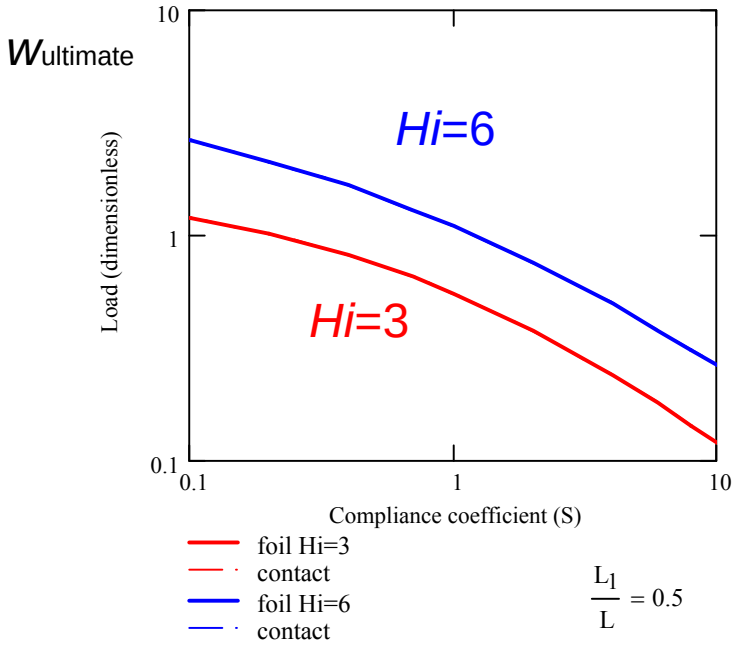

Fig. 27 Ultimate load capacity versus compliance (S) for two inlet films. Tapered length L_1/L=0.5

The results demonstrate the ultimate load capacity of a (simple) compliant gas bearing with non-zero film thickness. Unlike incompressible fluid (liquid) bearings, gas bearings do have a limited load capacity solely determined by the bearing geometry, the inlet and outlet film thicknesses, and the compliance parameter. The results in Figs. 27 and 28 are then used to estimate the operating film thickness since for a desired $\underline{S}$ parameter, and given the bump strip stiffness, then $h_* = p_a / k_b \underline{S}$.

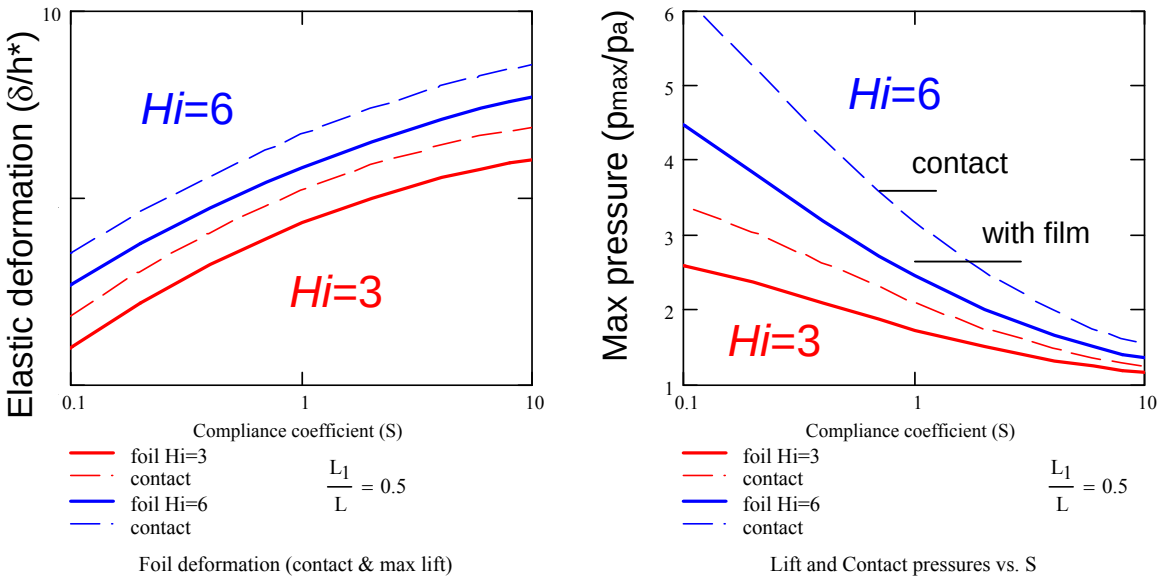

Fig. 28 Foil elastic deformation and maximum (contact and lift) pressures versus compliance parameter (*S*) for two inlet film conditions

Figure 29 shows the predicted pressure field on the bearing surface for rigid (*S*=*0*) and compliant (*S*=*3*) surface bearings at a finite speed condition (Λ=50). The figure also contains the contact pressure for operation without a hydrodynamic film (Λ=0). The predicted gas pressures correspond to numerical solutions of Eq. (51) using a fast, accurate and stable algorithm for thin gas films [8]. The predictions correspond to a load w=0.25, just 20 % below the ultimate load for the compliant surface bearing. Note the more uniform pressure distribution for the foil gas bearing on the non-tapered portion of the bump foil strip layer.

Figure 30 displays the predictions of load capacity (w) and minimum film thickness versus speed number (Λ) for a rigid (*S*=0) and compliant surface bearings (*S*=3, 6). At low speeds, the load is nearly proportional to surface speed, though it soon levels off and reaches the ultimate[20] load capacity for Λ>100. Note that the predictions based on the simple design formulae, Figs. 27 and 28, match perfectly those of the numerical predictions at high speed numbers.

[20] Some foil bearing providers erroneously claim ever increasing load capacities as Λ (surface speed) increases. The claim has no scientific grounds and merely reflects the commercial aspect of an emerging technology.

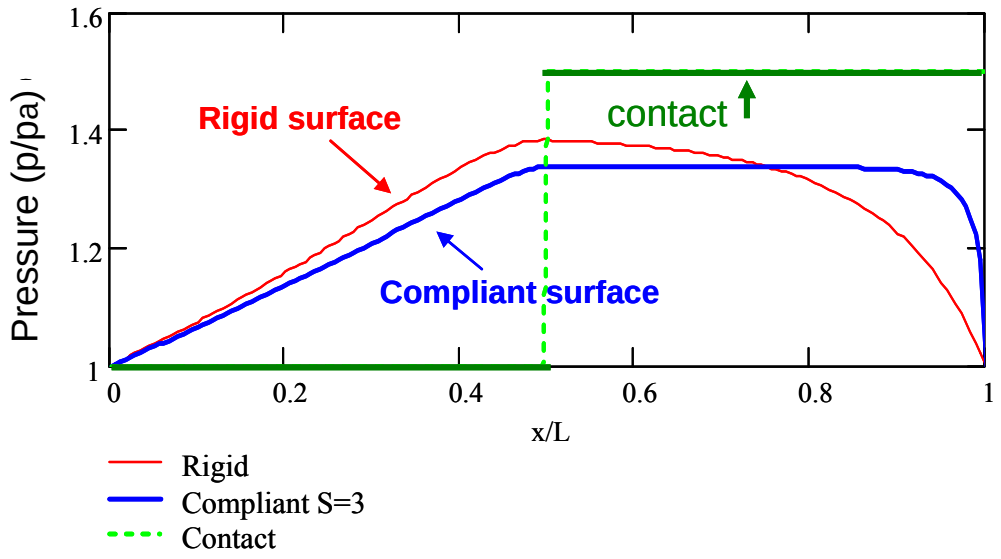

Fig. 29 Pressure field on bearing surface for speed number Λ=50. Rigid and compliant (*S*=3) surface bearings with H_i =3, *w*=0.25, and contact pressure at Λ=0

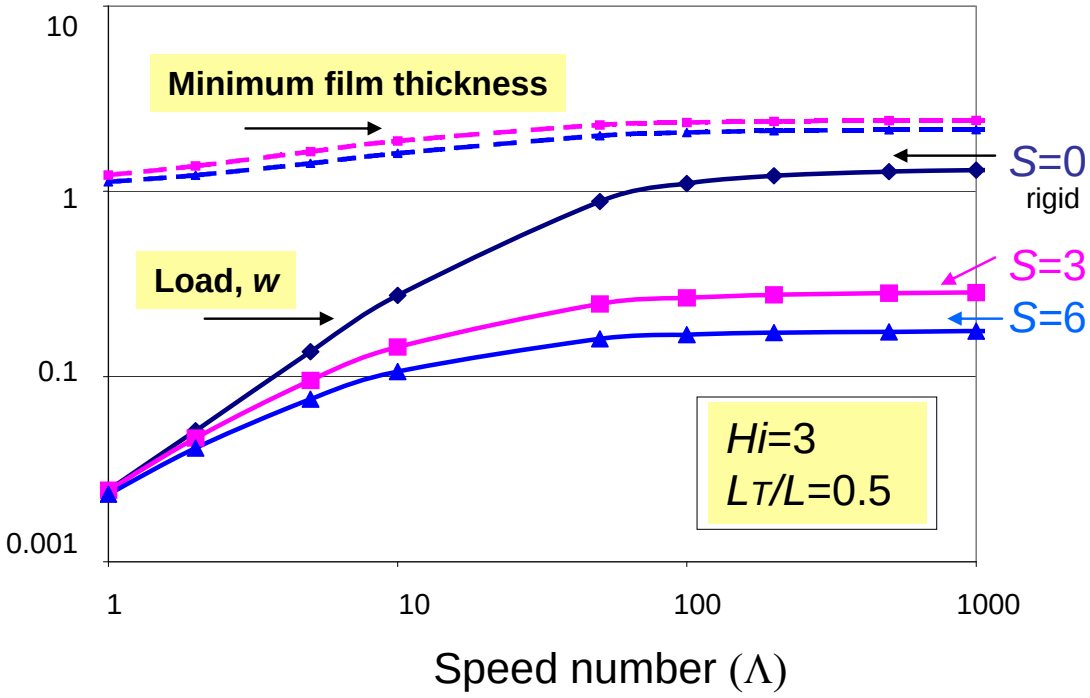

Fig. 30 Load capacity (*w*) and minimum film thickness versus speed number (Λ) for rigid (*S*=0) and compliant surface bearings (*S*=3, 6). H_i =3.

Dynamic force coefficients representative of small amplitude motions about an equilibrium condition are of importance to determine the dynamic forced response and stability of a mechanical system. Figure 31 depicts the predicted (dimensionless) stiffness and damping coefficients for rigid ($\underline{S}$=0) and compliant surface ($\underline{S}$=3) bearings at Λ=50, with film inlet H_i=3 and load w=0.25. The force coefficients are displayed as functions of increasing frequency numbers (σ), i.e. as the excitation frequency grows, and two loss factors, γ= 0 and 1, representative of low and high values of material damping within a foil bump strip, respectively.

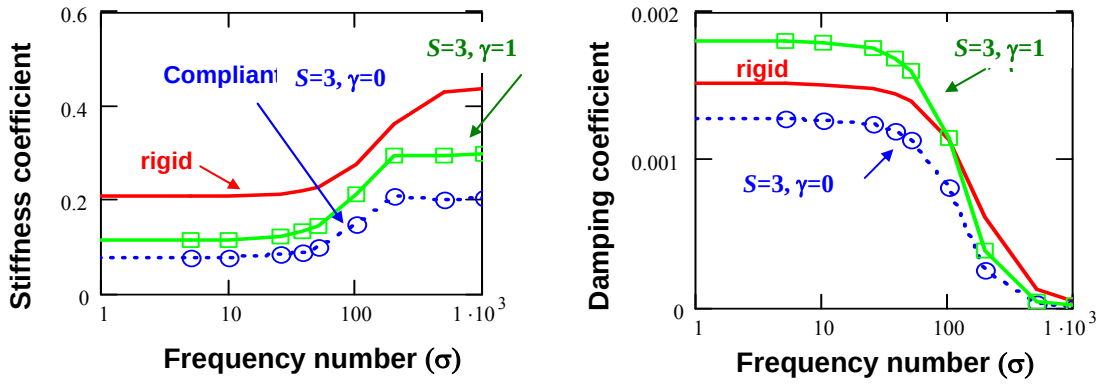

Fig. 31. Stiffness and damping force coefficients for rigid and compliant surface bearings versus frequency number (σ). Effect of loss factor (γ) on dynamic force coefficients. H_i=3, Λ=50, w=0.25

The stiffness coefficient (K_B) shows a typical hardening effect as the frequency of excitation grows, while the damping coefficient (C_B) decreases rapidly. However, the compliant surface bearing with a large loss factor (γ=1) has more damping capability than the rigid surface bearing. The results demonstrate that foil bearings may be tuned (designed) to give desirable dynamic force characteristics to control the placement of critical speeds and enhanced damping in operating regions of interest.

Ref. [14] shows a similar (simple) analysis giving the limit or ultimate load capacity of radial foil bearings.

Considerations on foil bearings for oil-free turbomachinery

Until recently GFB design was largely empirical, each foil bearing being a custom piece of hardware, with resulting variability even in identical units, and limited scalability. At present,

the advances in radial GFB technology (design, construction and predictability) permit OEMs and end users to implement radial GFBs for deployment into novel MTM or to upgrade and improve outdated rotating machinery. That is, there is enough published know-how on materials, guidelines for design and construction of radial GFBS including engineered coatings for high temperature applications, a reliable data base of GFB forced performance (static and dynamic), and computational tools benchmarked to test data.

Research on radial GFBs for lateral support of oil-free rotating machinery has steadily progressed with comprehensive analyses accounting for most relevant physical aspects to accurately predict GFB static and dynamic load performance, power loss, and the management of thermal energy in high temperature applications. Empirical research has gone beyond showing a few instances of acceptable mechanical performance, to demonstrate GFB multiple-cycle repeatable performance in spite of persistent large amplitude whirl motions at low frequencies, typically coinciding with the system natural frequencies. Many developmental efforts have attempted to fix or suppress these undesirable motions. One could hastily attribute the sub harmonic whirl motions to a typical rotordynamic instability induced by hydrodynamic effects of the gas film, i.e. generation of too large cross-coupled stiffness coefficients that destabilize the rotor-bearing system. However, as learned from the measurements [29], rotor imbalance triggers and exacerbates the severity of subsynchronous motions. The subsynchronous behavior is a forced nonlinearity due to the foil bearing strong nonlinear (hardening) stiffness characteristics, as is demonstrated in Ref. [30]. The predictions and measurements validate the simple FB model, i.e. a minute gas film with effective *infinite* stiffness, with applicability to large amplitude rotordynamic motions.

Challenges for gas FBs include intermittent contact and wear at startup and shut down, and potential for large amplitude rotor whirl at high speeds. Subsynchronous motions are common in FBs due to their strong structural hardening nonlinearity. Incidentally, the ultimate load capacity of a gas foil bearing depends mainly on its support structure. Hence, engineers must pay close attention to the bearing structural components (design, fabrication and assembly).

Luis San Andrés, Mast-Childs Professor
Texas A&M University, Turbomachinery Laboratory
First draft: August 2010, Revision: February 2012

References

[1] Gross W.A., 1962, *Gas Film Lubrication*, John Wiley & Sons, Inc. NY.

[2] Pan, C.H.T., 1980, "Gas Bearings," *Tribology: Friction, Lubrication and Wear*, Edited by A.Z. Szeri, Hemisphere Pub. Corp., Wa

[3] Hamrock, B.J., 1994, *Fundamentals of Fluid Film Lubrication,* Chaps. 16-17, McGraw-Hill, Inc., NY.

[4] Czolczynski, K., 1999, *Rotordynamics of Gas-Lubricated Journal Bearing Systems*, Springer Verlag, Inc., NY.

[5] DellaCorte, C., Radil, K. C., Bruckner, R. J., and Howard, S. A., 2008, "Design, Fabrication, and Performance of Open Source Generation I and II Compliant Hydrodynamic Gas Foil Bearings", STLE Tribol. Trans., **51,** pp. 254-264

[6] Belforte, G., Raparelli, T., Viktorov, V., Trivella, A., and Colombo, F., 2006, "An experimental study of high-speed rotor supported by air bearings: test rig and first experimental results", Tribology International, Vol. 39, pp. 839-845

[7] Zirkelback, N., and L. San Andrés, 1999, "Effect of Frequency Excitation on the Force Coefficients of Spiral Groove Thrust Bearings and Face Gas Seals," ASME Journal of Tribology, Vol. 121, 4, pp. 853-863.

[8] Faria, M., and L. San Andrés, 2000, "On the Numerical Modeling of High Speed Hydrodynamic Gas Bearings," ASME Journal of Tribology, Vol. 122, 1, pp. 124-130

[9] San Andrés, L., and D. Wilde, 2001, "Finite Element Analysis of Gas Bearings for Oil-Free Turbomachinery," Revue Européenne des Eléments Finis, Vol. 10 (6/7), pp. 769-790

[10] San Andrés, L., 2006, "Hybrid Flexure Pivot-Tilting Pad Gas Bearings: Analysis and Experimental Validation," ASME Journal of Tribology, 128, pp. 551-558.

[11] Wilde, D.A., and San Andrés, L., 2006, "Experimental Response of Simple Gas Hybrid Bearings for Oil-Free Turbomachinery," ASME Journal of Engineering for Gas Turbines and Power, 128, pp. 626-633

[12] Zhu, X., and L. San Andrés, 2005, "Experimental Response of a Rotor Supported on Rayleigh Step Gas Bearings," ASME Paper GT 2005-68296

[13] San Andrés, L., and Ryu, K., 2008, "Hybrid Gas Bearings with Controlled Supply Pressure to Eliminate Rotor Vibrations while Crossing System Critical Speeds," ASME Journal of Engineering for Gas Turbines and Power, Vol. 130(6), pp. 062505-1-10

[14] Kim, T.H., and L. San Andrés, 2006, "Limits for High Speed Operation of Gas Foil Bearings," ASME Journal of Tribology, 128, pp. 670-673.

[15] Kim, T.H., and L. San Andrés, 2008, "Heavily Loaded Gas Foil Bearings: a Model Anchored to Test Data," ASME Journal of Engineering for Gas Turbines and Power, Vol. 130(1), pp. 012504

[16] San Andrés, L., and Kim, T.H., 2009, "Analysis of Gas Foil Bearings Integrating FE Top

Foil Models," Tribology International, **42**(2009), pp. 111-120

[17] Carnes, C., 2004, "Hard-driving Lubrication," Tribology & Lubrication Technology, Nov., pp. 32-38

[18] Chen, H. M., Howarth, R. Geren, B., Theilacker, J. C., and Soyars, W. M., 2000, "Application of Foil Bearings to Helium Turbocompressor," Proc. 30th Turbomachinery Symposium, Turbomachinery Laboratory, Texas A&M University, Houston, TX, pp. 103-113.

[19] San Andrés, L., Chirathadam, T., Ryu, K., and Kim, T.H., 2010, "Measurements of Drag Torque, Lift-Off Journal Speed and Temperature in a Metal Mesh Foil Bearing," ASME J. Eng. Gas Turbines Power, 132 (in print)

[20 Childs, D., 1993, *Turbomachinery Rotordynamics,* Chap.5, "Rotordynamic Models for Annular Gas Seals," John Wiley & Sons, Inc., NY

[21] Szeri, A. Z., 1998, *Fluid Film Bearings: Theory & Design*, Chap. 11, Cambridge University Press, UK.

[22] San Andrés, L., 2006, Modern Lubrication Theory, "One Dimensional Slider Bearing, Rayleigh Step Bearing, and Circular Plate Squeeze Film Damper," Lecture Notes No. 2, Open source: http://rotorlab.tamu.edu/me626

[23] Lund, J. W., 1968, "Calculation of Stiffness and Damping Properties of Gas Bearings," ASME J. Lubr. Tech., 90, pp. 793-803.

[24] Lund, J. W., 1967, "A Theoretical Analysis of Whirl Instability and Pneumatic Hammer for a Rigid Rotor in Pressurized Gas Journal Bearings," ASME J. Lubr. Tech., **89**, pp. 154-163.

[25] Lund, J.W., 1965, "The Stability of an Elastic Rotor in Journal Bearings with Flexible Damped Supports," ASME Journal of Applied Mechanics, p. 911-920.

[26] San Andrés, L., and Ryu, K., 2008, "Hybrid Gas Bearings with Controlled Supply Pressure to Eliminate Rotor Vibrations while Crossing System Critical Speeds," ASME J. Eng. Gas Turbines Power, **130**(6), pp. 062505 (1-10)

[27] San Andrés, L., Niu, Y., and Ryu, K, "Dynamic Response of a Rotor-Hybrid Gas Bearing System Due To Base Induced Periodic Motions," ASME paper GT2010-22277

[28] Dykas, B., Bruckner, R., DellaCorte, C., Edmonds, B., Prahl, J., 2009, "Design, Fabrication, and Performance of Foil Gas Thrust Bearings for Microturbomachinery Applications," ASME J. Eng. Gas Turbines Power, **131**, p. 012301

[29] San Andrés, L., Rubio, D., and Kim, T.H, 2007, "Rotordynamic Performance of a Rotor Supported on Bump Type Foil Gas Bearings: Experiments and Predictions," ASME J. Eng. Gas Turbines Power, **129,** pp. 850–857

[30] San Andrés, L., and Kim, T.H., 2008, "Forced Nonlinear Response of Gas Foil Bearing Supported Rotors," Tribology International, **41**(8), pp. 704-715

Nomenclature

B	Bearing width [m]
c	Radial clearance in journal bearing [m]
c_P	Machined clearance in a tilting pad bearing [m]
$C_{\alpha\beta}$	Damping coefficients [N·s/m]; $_{\alpha\beta=X,Y}$. $\underline{C}_{\alpha\beta}= C_{\alpha\beta}/C_*$
C_*	$\mu \frac{D}{4}\left(\frac{L}{c}\right)^3$. Factor for damping coefficient in radial bearing
$\bar{C}$	$\frac{C}{12\,\mu\, B\left(L_*/h_*\right)^3}$ Dimensionless damping coefficient (slider bearing)
d	Orifice diameter in externally pressurized bearing [m]
D	Journal or rotor diameter [m]
e_X, e_Y	Components of journal eccentricity vector [m]. $\varepsilon=e/c$
F_X, F_Y	Components of bearing reaction force [N].
f	T_{orque}/cW. Drag friction coefficient in journal bearing
h	Film thickness [m].
H	h/h_*, h/c. Dimensionless film thickness
$K_{\alpha\beta}$	Damping coefficients [N·s/m]; $_{\alpha\beta=X,Y}$. $\underline{K}_{\alpha\beta}= K_{\alpha\beta}/K_*$
K_*	$C_*\Omega$. Factor for stiffness coefficient in radial bearing
$\bar{K}$	$\frac{K}{B\,L\,p_a/h_*}$ Dimensionless stiffness coefficient (slider bearing)
k_b	Foil bearing stiffness/unit area [N/m/m^2]
Kn	(λ/h). Knudsen number. > 15 for continuum flow.
L	Length of bearing [m]
M_P	Pad moment [Nm]
$\dot{m}_{OR}$	Orifice mass flow rate [kg/s]
M	Rigid rotor mass [kg]
M_c	Critical mass of rigid rotor-bearing system [kg]
N	Rotational speed [rev/s]
n_{pe}	Number of nodes in finite element
p	Pressure [Pa]. $P=p/p_a$
p_a, p_S	Ambient and supply pressures [Pa]
p_0, p_1	Zeroth and first order pressure fields. [Pa], [Pa/m]
q_η	Flow normal to an element
r_P	Machined preload in a multiple pad and tilting pad bearings [m]
R	½ D. Journal radius
Re	$\rho U h/\mu$. Shear flow Reynolds number
$\Re_g$	Gas constant [J/kg·K]
S	Sommerfeld number. $S=\frac{\mu N L D}{W}\left(\frac{R}{c}\right)^2$
$\underline{S}$	$(s\, p_a/h_*)$. Foil bearing compliance number

s	$\frac{1}{k_b\left(1+i\,\eta\right)}$ Foil bearing compliance parameter [m^3/N]
$\underline{s}$	$s=\lambda \pm i\,\varpi$. Eigenvalue of characteristic equation
t	Time [s]
T	Temperature [K]
T_{orque}	Drag torque [Nm]
U	Surface speed [m/s]. ΩR in journal bearing
W	Load [N]. $w= W/(BLp_a), W/(LDp_a)$
W_X, W_Y	Components of load acting on bearing [N].
WFR	(ϖ/Ω). Whirl frequency ratio
X,Y	Inertial coordinate system for journal bearing analysis
x, y, z	Coordinate system in plane of bearing
$\mathbf{z}$	$\{x_{(t)}\ ,y_{(t)}\}^{\mathrm{T}}$. Vector of journal center dynamic displacements [m]
Z	Complex impedance [N/m]; $Z = (K + i\ \omega C),\ i=\sqrt{-1}$
Δy	Small amplitude motion [m]
Δe_X, Δe_Y	Small amplitude journal center motions [m]
α	(h_1/h_2). Ratio of inlet to outlet film thickness in slider bearing
γ	(L_2/L). Ratio of lengths in Rayleigh step and tapered-flat slider bearings
γ	Material loss coefficient in foil bearing
κ	Gas specific heats ratio
Γ^e	Element boundary
ϕ	Angle between load vector and journal eccentricity vector [deg]
τ	ωt. Dimensionless time
δ, ξ, η	Coordinates for pad tilt, radial and transverse displacements
ε	(e/c). Journal eccentricity ratio
Θ	x/R. Circumferential coordinate fixed to stationary
Θ_P	Angular location of pad pivot
λ	Gas molecular free path [m]
Λ	Speed number. $\Lambda = \frac{6\,\mu U\,L_*}{p_a\,h_*^2}$, $\Lambda = \frac{6\,\mu\,\Omega}{p_a}\left(\frac{R}{c}\right)^2$
μ	Gas viscosity [Pa·s]
ρ	Gas density [kg/m^3]
σ	Frequency number. $\sigma = \frac{12\,\mu\,\omega\,L_*^2}{p_a\,h_*^2} = \Lambda\,\frac{\omega}{\frac{1}{2}\Omega}$
$\left\{\Psi_i\right\}_{=1}^{n_{pe}}$	Shape functions within the finite element
ω	Frequency of dynamic motions [rad/s]
ϖ	Whirl frequency of unstable dynamic motions [rad/s]
Ω	($2\pi N$). Rotor or journal speed [rad/s]

Ω^e	Finite element sub-domain

Subscripts

o	Zeroth-order
1	First-order
*	Characteristic value
P	Pad
u	Ultimate limit at $\Lambda \to \infty$

Acronyms

FPTPB	Flexure pivot tilting pad bearing
GFB	Gas foil bearing
RBS	Rotor-bearing system

Appendix Numerical solution of Reynolds equation for gas films

There are numerous methods for the numerical solution of the gas film Reynolds equation, including finite differences, finite elements, control-volume methods and boundary element methods. Prior to 1990, finite difference methods were favored. However, into the present day, the finite element method has gained in popularity because of its ability to seamlessly tackle complex configurations, including textured (spiral groove) geometries, and including supply ports. However, recall that the compressible fluid Reynolds equation is non linear, hence requiring of iterative methods – Newton-Raphson like- to achieve convergence to a unique solution. Moreover, the character of the equation changes from elliptical to hyperbolic as the speed or frequency (numbers) increase. As the literature extensively reports, predictions under these conditions using central difference schemes of finite elements with linear interpolation functions show numerical oscillations and eventually numerical instability.

Fortunately, nowadays there is a method that avoids such difficulties by using interpolation or shape (analytical) functions that seamlessly transition from elliptic to parabolic flow conditions as the speed increases. See Ref. [8] for this important development that allows prediction of gas film static and dynamic force characteristics for arbitrarily high-speed gas bearing numbers.

The flow domain in a pad is divided into four-noded rectangular finite elements $\Omega_e : \left\{ l_x^e = \frac{1}{N_x}, l_y^e = \frac{L/L_x}{N_y} \right\}$ where (N_x, N_y) is the global number of elements in the circumferential and axial directions, respectively. Within an element the zeroth- and first-order pressures are functions of the nodal pressures and shape functions $\{\psi_i^e\}_{i=1..4}$, i.e.,

$$P_0^e = \sum_{i=1}^{4} \psi_i^e \bar{P}_{0_i}^e,\ P_\alpha^e = \sum_{i=1}^{4} \psi_i^e \bar{P}_{\alpha_i}^e;\ _{\alpha=X,Y} \qquad \text{(A.1)}$$

These equations are substituted into the Reynolds equation, which is further multiplied by an identical set of weight functions and integrated over an element domain. The Petrov-Galerkin method leads to the following set of zeroth- and first-order finite element equations (not including a source of external pressurization)

$$k_{ji}^e \bar{P}_{0_i}^e = r_j^e + q_j^e;$$

$$k_{\alpha_{ji}}^e \bar{P}_{\alpha_i}^e = r_{\alpha_j}^e + q_{\alpha_j}^e\ ;\ _{i,j=1..4;\alpha=X,Y} \qquad \text{(A.2)}$$

where $$k^e_{ji} = \iint_{\Omega_e} \left[\bar{P}^e_o \, H^3_o \left(\psi^e_{i,x} \psi^e_{j,x} + \psi^e_{i,z} \psi^e_{j,z} \right) - \Lambda \, H_o \psi^e_i \, \psi^e_{j,x} \right] d\Omega_e ,$$

$$r^e_j = 0 ; \qquad q^e_j = -\oint_{\Gamma_e} \psi^e_j \, \dot{m}^e_\eta \, d\Gamma_e \tag{A.3}$$

and

$$k^{\;e}_{\alpha ji} = \iint_{\Omega_e} \begin{bmatrix} \bar{P}^e_0 \, H^3_0 \left(\psi^e_{i,\bar{x}} \psi^e_{j,\bar{x}} + \psi^e_{i,\bar{y}} \psi^e_{j,\bar{y}} \right) + \psi^e_i \, H^3_0 \left(\bar{P}_{o,\bar{x}} \psi^e_{j,\bar{x}} + \bar{P}_{o,\bar{y}} \psi^e_{j,\bar{y}} \right) \\ - \Lambda \, H_0 \psi^e_i \, \psi^e_{j,\bar{x}} + i \sigma \, H_0 \psi^e_i \, \psi^e_j \end{bmatrix} . d\Omega_e$$

$$r^{\;e}_{\alpha j} = -\iint_{\Omega_e} \left[3 \bar{P}^e_0 \, H^2_0 \left(\bar{P}_{0,\bar{x}} \psi^e_{j,\bar{x}} + \bar{P}_{0,\bar{y}} \psi^e_{j,\bar{y}} \right) - \Lambda \, \bar{P}_o \psi^e_{j,\bar{x}} + i \sigma \, \bar{P}_0 \psi^e_j \right] . d\Omega_e \tag{A.4}$$

$$q^e_{\alpha_j} = -\oint_{\Gamma_e} \psi^e_j \dot{m}^e_{\alpha_\eta} d\Gamma_e$$

$\mathbf{k^e}$ represents the element fluidity matrix, and $\mathbf{r^e}$ and $\mathbf{q^e}$ denote the vectors of shear and squeeze flows, and nodal mass fluxes ($\dot{m}^e_\eta$) through the element boundary Γ_e, respectively.

Within a finite element $\Omega_e : \left\{ \bar{x}^e \cong \frac{(\xi+1)}{2} l^e_x , \bar{y}^e \cong \frac{(\eta+1)}{2} l^e_y \right\}$, and natural coordinates $\{\xi, \eta\} \in [-1, +1]$, the advanced shape functions are [8]

$$\psi^e_1 = \frac{1}{2}(1-\eta)\left(\frac{e^{\lambda_e} - e^{\lambda_e \xi}}{e^{\lambda_e} - e^{-\lambda_e}} \right); \qquad \psi^e_2 = \frac{1}{2}(1-\eta)\left(\frac{e^{\lambda_e \xi} - e^{-\lambda_e}}{e^{\lambda_e} - e^{-\lambda_e}} \right)$$

$$\psi^e_3 = \frac{1}{2}(1+\eta)\left(\frac{e^{\lambda_e \xi} - e^{-\lambda_e}}{e^{\lambda_e} - e^{-\lambda_e}} \right); \qquad \psi^e_4 = \frac{1}{2}(1+\eta)\left(\frac{e^{\lambda_e} - e^{\lambda_e \xi}}{e^{\lambda_e} - e^{-\lambda_e}} \right) \tag{A.5}$$

where $\lambda_e = \frac{\Lambda \, l^e_x}{P^e_o H^2_e}$ is a local Peclet number showing the ratio of convection (shear) flow to diffusion (Poiseuille) flow. At low bearing speed numbers ($\lambda_e \to 0$), the novel shape functions reduce to the well known bilinear interpolation functions. For high speed numbers where fluid convection dominates the film flow, $\lambda_e \to \infty$, the shape functions produce a full upwinding fluidity matrix with negligible diffusive terms (artificial viscosity)

Eq. (A.2) are constructed for each element, assembled over the flow domain, and then condensed by enforcing appropriate boundary conditions, including the source terms arising from any external (orifice) pressurization. The resultant global set of equations is

$$\mathbf{k}_{\mathbf{G}}\,\bar{\mathbf{P}}_{\mathbf{o}_{\mathbf{G}}} = \mathbf{Q}_{\mathbf{o}_{\mathbf{G}}} + \mathbf{R}_{\mathbf{o}_{\mathbf{G}}} \tag{A.6}$$

where $\mathbf{k}_{\mathbf{G}} = \bigcup_{e=1}^{Nem} \mathbf{k}^{\mathbf{e}}; \mathbf{R}_{\mathbf{G}} = \bigcup_{e=1}^{Nem} \mathbf{r}^{\mathbf{e}}; \mathbf{Q}_{\mathbf{o}_{\mathbf{G}}} = \bigcup_{e=1}^{Nem} \mathbf{q}^{\mathbf{e}} + \mathbf{q}^{\mathbf{sources}}$ for the equilibrium pressure field. A similar equation set follows for the first-order pressure fields. The asymmetric global fluidity matrix $\mathbf{k}_{\mathbf{G}}$ is nonlinear since its elements depend on the zero$_{th}$-order pressure field ($\bar{\mathbf{P}}_{\mathbf{o}_{\mathbf{G}}}$).

Earlier developments relied on the continuous evaluation, assembly and decomposition of the global fluidity matrix. Presently, a line solver with successive under-relaxation is used. The procedure assembles the finite element equations along a line (constant axial coordinate) and solves them using the TDMA algorithm. The method is faster than the full matrix decomposition procedure since new pressures are immediately updated in the iterative procedure. Good convergence rates are found by selecting appropriate under relaxation factors (0.7 typically).

See Refs. [8-10] for further details on the method implementation, including external pressurization (supply ports) and tilting pad bearings.